Development of strain hardening cementitious composite (SHCC) reinforced with 3D printed polymeric reinforcement

Mechanical properties

Xu, Yading; Šavija, Branko

DOI
10.1016/j.compositesb.2019.107011

Publication date
2019

Document Version
Accepted author manuscript

Published in
Composites Part B: Engineering

Citation (APA)
Xu, Y., & Šavija, B. (2019). Development of strain hardening cementitious composite (SHCC) reinforced with 3D printed polymeric reinforcement: Mechanical properties. *Composites Part B: Engineering*, *174*, Article 107011. https://doi.org/10.1016/j.compositesb.2019.107011

Development of Strain Hardening Cementitious Composite (SHCC) reinforced with 3D printed polymeric reinforcement: mechanical properties

Yading Xu, Branko Šavija

Microlab, Delft University of Technology, Delft, Netherlands

Abstract

Cracking in concrete needs to be limited for esthetical and durability reasons. Currently, this is commonly done by using steel rebars in the structure or fiber reinforcement in the material. With certain fiber types and micromechanical design, it is even possible to create cement-based materials with steel like (i.e. quasi-plastic) properties – so called strain hardening cementitious composites (SHCCs). In this paper, an alternative approach for creating SHCC – through use of additive manufacturing to create polymeric reinforcement meshes – is proposed. Different designs are manufactured, casted in the cementitious matrix, and tested in four-point bending and uniaxial tension. It was found that, with proper designs, it is possible to create cementitious composites with deflection hardening or strain hardening properties. Furthermore, with proper design, multiple cracking behavior of conventional SHCC can be replicated. In addition, numerical simulations were performed using the Delft lattice model. Four point bending tests on mortar bars reinforced by two different mesh designs were simulated and the results show good agreement with the experiments. This research shows great potential of using additive manufacturing for creating SHCCs with customizable properties.

Key words: *Strain hardening cementitious composite; 3D printing; Polymeric reinforcement, Delft lattice model.*

1. Introduction

Concrete is the most widely used construction material in the world. Compared to other construction materials, such as e.g. steel and timber, concrete structures are more resistant to aggressive environmental conditions. However, while concrete shows excellent resistance to compressive loads, it is relatively weak in tension. Therefore, steel reinforcement is added to take over the tensile loads. Reinforcing steel is, in general, protected from corrosion by a passive film that forms around it in an alkaline environment of the concrete pore solution

[1]. Over the lifetime of a structure, this protective film might break down due to carbonation [2, 3] or chloride ingress [1, 4]. Once this happens, active corrosion of the reinforcement will start, causing loss of steel cross section [5] and, eventually, cracking [6], and spalling of the concrete cover [7]. Therefore, it is important that the quality of the concrete cover is ensured to protect the reinforcement. However, reinforced concrete structures are commonly cracked. Wide cracks present fast pathways for moisture [8], carbon dioxide [9] and chloride ingress [10, 11], resulting in fast corrosion initiation and end of service life [12]. Therefore, limiting crack width is crucial to ensuring the durability of reinforced concrete structures.

The weak tensile response of concrete can be overcome by the addition of fibers to the material [13]. Commonly used fiber types include steel [14], glass [15] and natural fibers [16]. The role of fiber reinforcement is mainly to increase the fracture toughness, prevent crack localization, and reduce the crack width in concrete. Furthermore, in recent decades, a new class of fiber reinforced concrete – strain hardening cementitious composite (SHCC) – has been developed. SHCC is a class of ultra-ductile fiber reinforced composites developed in the early 1990s [17]. It is characterized by a large strain capacity (sometimes more than 5%) and a strain hardening behavior in tension achieved through tightly spaced distributed microcracking [18]. Typically, SHCCs are reinforced with a relatively small amount (around 2% by volume) of polyvinyl alcohol (PVA) fibers [19, 20], although other fiber types such as polyethylene have also been used [21]. Practical application of fiber reinforcement in concrete is not without problems – fiber orientation is influenced by execution parameters, such as the size of the structural member and the direction of the concrete flow during casting [22, 23]. Furthermore, agglomeration of fibers and weak spots in the material may occur. This can be overcome to a certain extent by using a pre-fabricated reinforcement, as is the case in textile reinforced concrete (TRC). TRC elements typically consist of several layers of textile fabrics of multi-filament yarns made of alkali- resistant glass or carbon, which are embedded in a fine-grained concrete or mortar [24]. Similar to SHCC, TRC shows strain hardening and multiple cracking in tension [25]. It is therefore a viable alternative to SHCC.

In recent years, an alternative approach for creating complex geometries that may be used as micro-scale reinforcement in concrete has emerged. Recent developments in additive manufacturing (3D printing) [26] techniques for polymers (e.g. fused deposition modelling

[27, 28]) enable creating complex geometries. Reinforcement meshes created using additive manufacturing techniques could be used to replace fiber reinforcement. Although in the field of civil engineering most attention has been given to 3D printing of complete concrete structures [29] and structural reinforcement cages [30], recently attention has been given to printing reinforcement. Farina et al. [31] used additive manufacturing to create polymeric and metallic reinforcement for mortar elements subjected to bending. In their study, additive manufacturing was used to control the surface roughness of the reinforcement. Nam et al.[32] used fused deposition modelling to create structures to replace conventional fiber reinforcement in mortar in order to avoid problems associated with conventional fiber reinforcement such as e.g. fiber clustering. Rosewitz et al.[33] used 3D printed bio-inspired polymeric structures as reinforcement for cement mortar to enhance the performance of cementitious material. These publications show that there is great potential in using additive manufacturing techniques for creating reinforcements which have potential to replace conventional fiber reinforcement.

Numerical simulations can be of great help in analyzing experimental trends. In previous studies [34, 35], lattice models were successfully used to simulate fracture processes of steel reinforced and fiber reinforced cementitious materials. The basic principle of the lattice model is to discretize a continuum to a lattice network that consists of truss or beam elements. In general, linear elastic properties are assigned to the lattice elements. As soon as a prescribed displacement or load is imposed on the lattice network, a set of linear elastic analyses is carried out. In each loading step, one critical element is removed when element stress exceeds its strength. Reaction load and displacement are recorded in each step and the analysis is repeated until the entire lattice system fails. Failed element represents micro cracks in the material, in this sense the load-displacement response and material cracking behavior can be simulated.

In this work, development of strain hardening cementitious composites (SHCCs) that use 3D printed polymeric meshes with two dimensional triangular patterns, instead of discrete fiber reinforcement is presented. Different reinforcement geometries are manufactured and tested in four-point bending and uniaxial tension. Furthermore, numerical simulations of the experiments are performed using the lattice model. The experiments and simulation results are then critically discussed and suggestions for future work are given.

2. Materials and method

2.1. Materials

Cementitious materials reinforced with 3D printed polymeric meshes have been fabricated. The matrix material was a fine-grained cementitious mortar containing CEM I 42.5 N and fly ash as binder materials, with a water-to-binder ratio of 0.33. The assumed mixture was used to develop SHCC in [36], meanwhile relatively high fluidity was achieved making it easier to fill the hollow cells of the printed reinforcement in this study. The mixture is listed in Table 1.

Table 1. Mixture design of the matrix material (g/l), adapted from [36]

CEM I 42.5 N	*Fly ash*	*Sand (0.125~0.250 mm)*	*Superplasticizer (Glenium 51)*	*Water*
550	650	550	2	395

Polymeric reinforcement meshes were manufactured using a commercially available FDM 3D printer Ultimaker 2+ (Figure 1). In FDM, the model is printed layer by layer, from the bottom up. As a result, overhangs may be difficult to print and result in poorer quality. Therefore, relatively simple mesh patterns were selected in this study, as described below. Acrylonitrile Butadiene Styrene (ABS) was used as the printing material (i.e. filament). ABS has excellent mechanical properties, interlayer adhesion, minimal warping, reliable bed adhesion and high alkaline resistance [37], which is important for use in cement-based materials.

Printing parameters may affect the mechanical properties of the resulting structure. Therefore, they are kept constant throughout this research. Printing parameters used are given in Table 2. Printing direction has a significant effect on the mechanical properties [37, 38]. Therefore, printing was performed in the direction parallel to the normal stress, resulting in maximum strength.

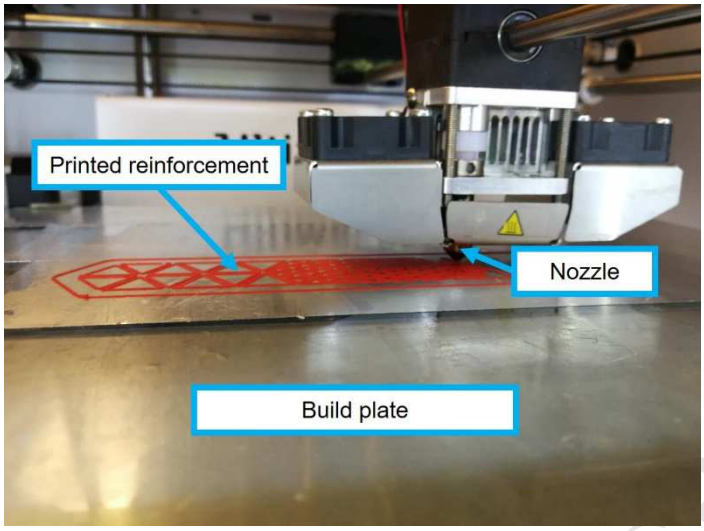

Figure 1 Schematics of reinforcement printing setup in the Ultimaker 2+.

Table 2. Printing parameters for reinforcement meshes used

Printing parameter	*Configuration*
Nozzle diameter (mm)	0.8
Temperature (°C)	260
Layer height (mm)	0.2
Line width (mm)	0.7
Infill density (%)	100
Infill pattern	Lines
Printing speed (mm/s)	40

2.2. Reinforcement designs

In this study, reinforcements with three different patterns were manufactured and tested. All patterns are based on triangular lattices, as shown in Figure 2 and Figure 3. As can be seen, different sizes of triangles are used, and the cross section of the reinforcement along the printed mesh is not constant. For small triangles, large triangles and mixed triangles the cross-sectional reinforcing ratio of different patterns is listed in Table 3 and the triangle pattern size parameters are shown in Figure 2d and Figure 2e. The small triangle pattern has an overall higher cross-sectional reinforcing ratio, therefore, it was expected that smaller triangle size (Figure 2b) will provide a better reinforcement effect compared to larger triangles (Figure 2a) and, as a result, better global behavior. The pattern in Figure 2c is a mix of the two previous patterns: large triangles are used in the outer parts of the mesh, while a

denser mesh is created in the middle. This pattern was used only in four-point bending tests. In four-point bending, the middle portion of the specimen is subjected to a constant bending moment, which is higher than the outer regions, and thus requires more reinforcement. In that case, additive manufacturing may be able to more optimally utilize the reinforcement compared to traditional textile or fiber reinforcement. Therefore, the pattern shown in Figure 2c was developed to test that it is possible to create a simple functionally graded material, in which the material structure (in this case, printed "fiber" reinforcement) is adjusted to the actual stress state, through use of additive manufacturing.

Table 3 Cross sectional reinforcing ratio of different reinforcement patterns

Reinforcement pattern	Cross sectional reinforcing ratio (%)
Large triangles	12.5 ~ 17.5
Small triangles	17.5 ~ 32.5
Mixed triangles	12.5 ~ 32.5

In addition to different patterns, roughness of the printed reinforcement mesh may have an effect on the bond and, consequently, the mechanical properties of the composite material. Therefore, for each of the loading conditions tested (i.e. four-point bending and uniaxial tension, respectively), one of the patterns was additionally roughened by introducing a rough profile on one side of the printed mesh as shown in Figure 3d (in order to avoid big overhangs during 3D printing which may result in poor printing quality, only the upper side of the mesh was printed with rough profile). These were mixed triangles pattern and the large triangles pattern for four-point bending and uniaxial tension experiments, respectively. A summary of all patterns and tests is given in Table 4. Note also that all reinforcement meshes were produced with "studs" that enabled the meshes to be easily positioned in the middle of the specimen during casting.

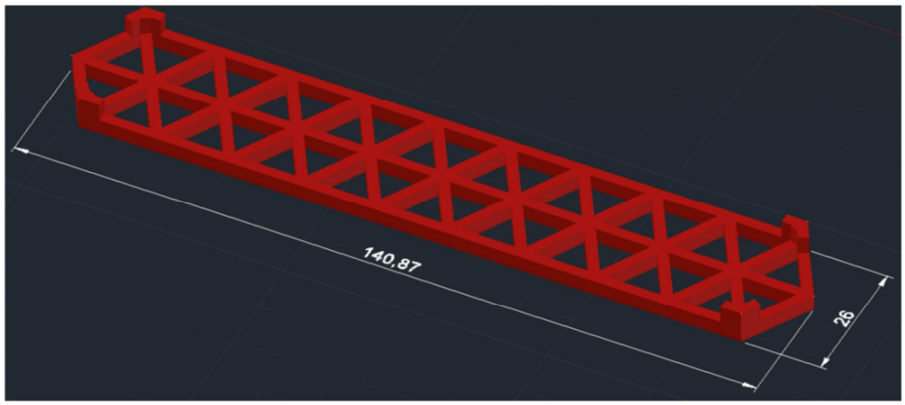

(a)

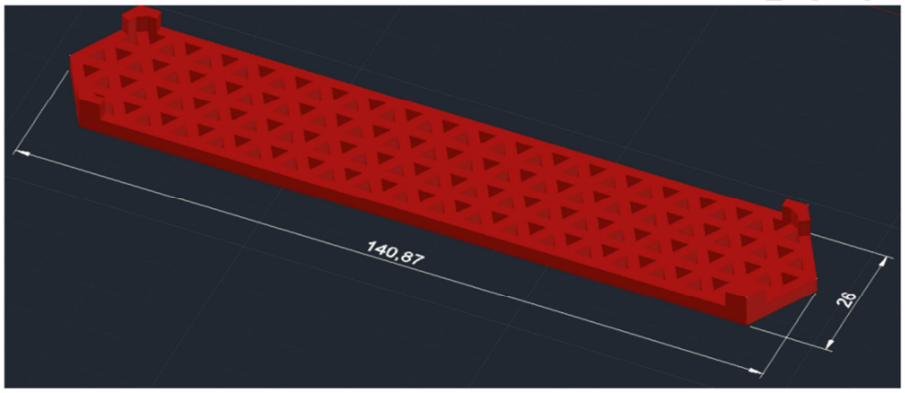

(b)

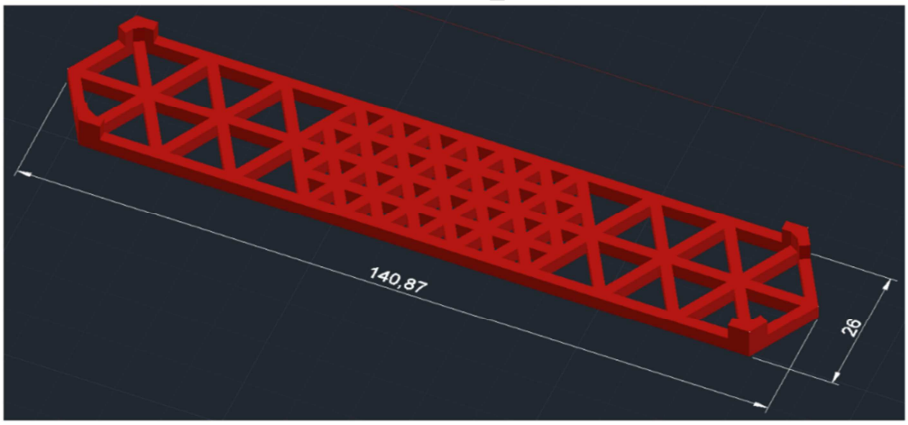

(c)

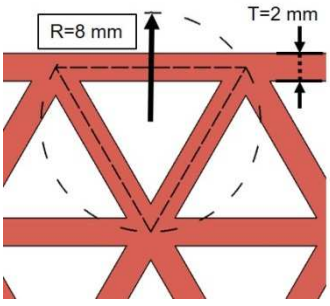

(d)

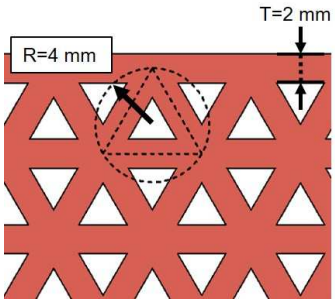

(e)

Figure 2. Design of polymeric reinforcement meshes and printed reinforcement. (a) large triangles;(b) small triangles; (c) mixed triangles (dimensions are in mm); (d) design parameters of large triangles; (e) design parameters of small triangles.

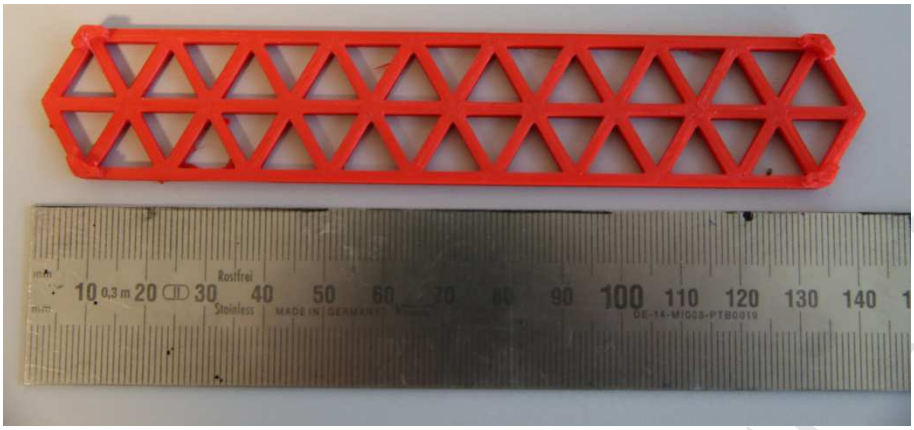

(a)

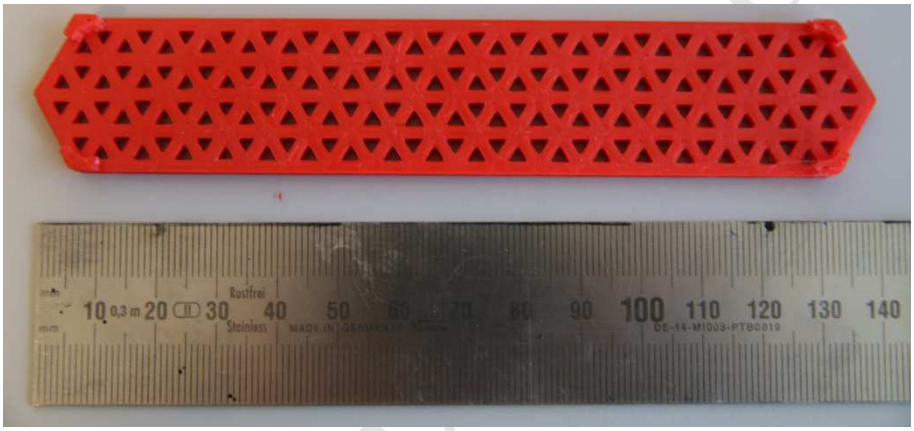

(b)

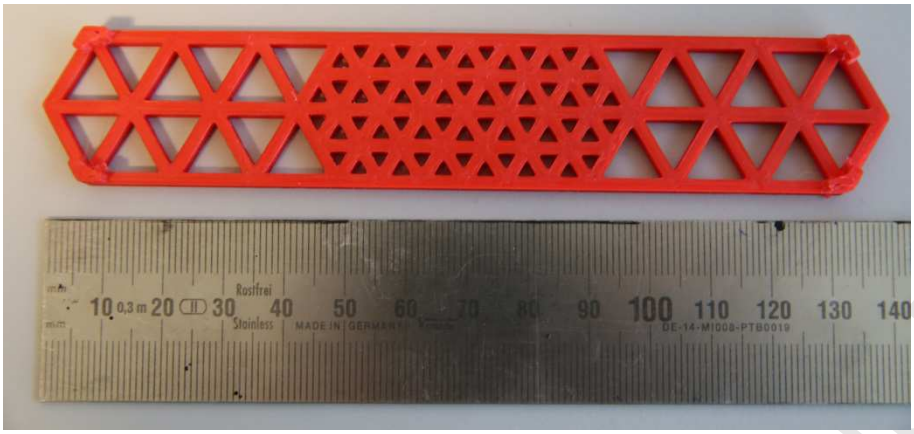

(c)

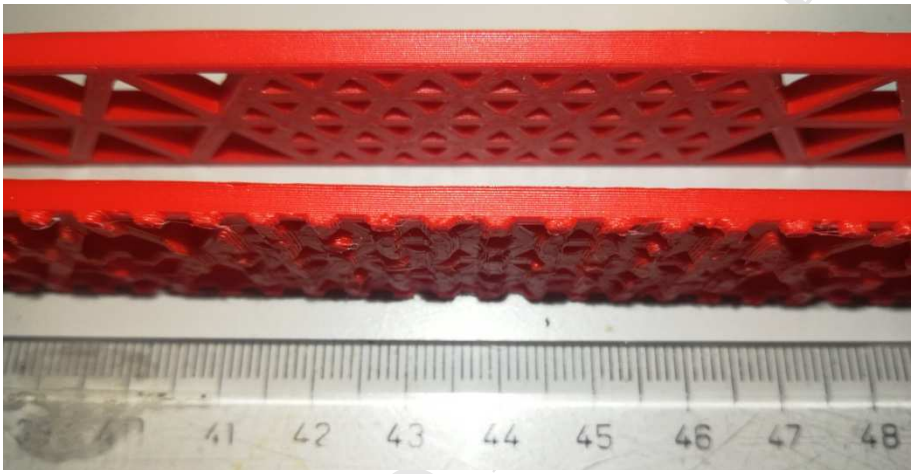

(d)

Figure 3. Printed reinforcement with (a) large triangle pattern; (b) small triangle pattern; (c) mixed triangle pattern; (d) smooth surface and rough surface

Table 4. A summary of all designs and tests

Triangle mesh type	Surface profile	Series ID	Diameter of cell circumscribed circle (mm)	Four-point bending	Uniaxial tension	Age
None	/	Ref, Ref_{28}	/	Yes	Yes	7d, 28d
Large	Smooth	LT	8	Yes	Yes	7d
Large	Rough	LT_R	8	No	Yes	7d
Small	Smooth	ST, ST_{28}	4	Yes	Yes	7d, 28d

Mixed	Smooth	MT, MT_{28}	4,8	Yes	No	7d, 28d
Mixed	Rough	MT_R	4,8	Yes	No	7d

178

179 ## 2.3. Casting and curing

180 The bottom surfaces of printed meshes were sanded for 30 seconds with 125µm sand paper
181 before casting to remove the glue layer in contact with 3D printer build plate. The positions
182 of reinforcement were marked on Styrofoam moulds. Then they were placed in Styrofoam
183 moulds (190 x 180 x 8 mm) with their studs pressed into the moulds for 1mm (shown in
184 Figure 4) and glued with silicone rubber to make sure the reinforcement stays in the middle
185 and does not move during vibration.

186

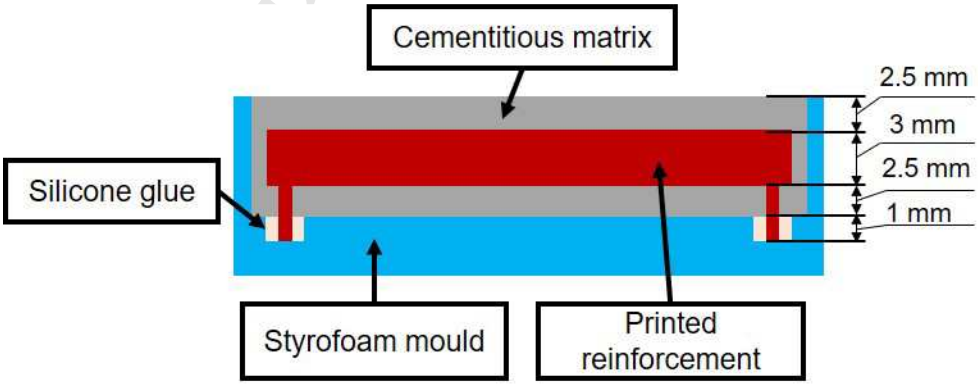

187

188 *Figure 4 Position of printed reinforcement in Styrofoam mould.*

189 The matrix materials were weighted according to the mix proportion given in Table 1. First,
190 solid ingredients were dry-mixed for four minutes in a Hobart laboratory mixer. After four
191 minutes, water and superplasticizer were added to the mixture and mixed for additional

four minutes. Subsequently, the materials were cast in the prepared moulds (with reinforcement already positioned) and vibrated for 30 seconds. Fresh specimens were covered with plastic sheets for one day (uniaxial tension) and two days (four-point bending), and then demoulded. After demoulding, they were placed in a curing room (20 ± 2°C, 96 ± 2%RH). Samples were cut to appropriate size for testing (described below) one day before testing.

2.4. Four-point bending test

Four-point bending tests were performed on cured samples using a servo hydraulic press (INSTRON 8872) under displacement control with a constant rate of 0.01mm/s. The load was measured by load cell and the deflection was measured by two linear variable differential transducers (LVDTs) placed at the mid-span. Specimen size used was 180 x 30 x 8 mm, with a loading span of 120 mm and loading applied as shown in Figure 5. A loaded specimen is shown in Figure 6. Note that the pattern given in Figure 2c was optimized for this loading setup: if a different loading setup were used, the middle region (i.e. the region with the maximum bending moment where a denser lattice mesh was printed) would have been different. For each specimen, flexural strength and flexural deflection capacity were determined as shown in Figure 7. For each configuration, at 7d four replicate specimens were tested and at 28d three replicate specimens were tested.

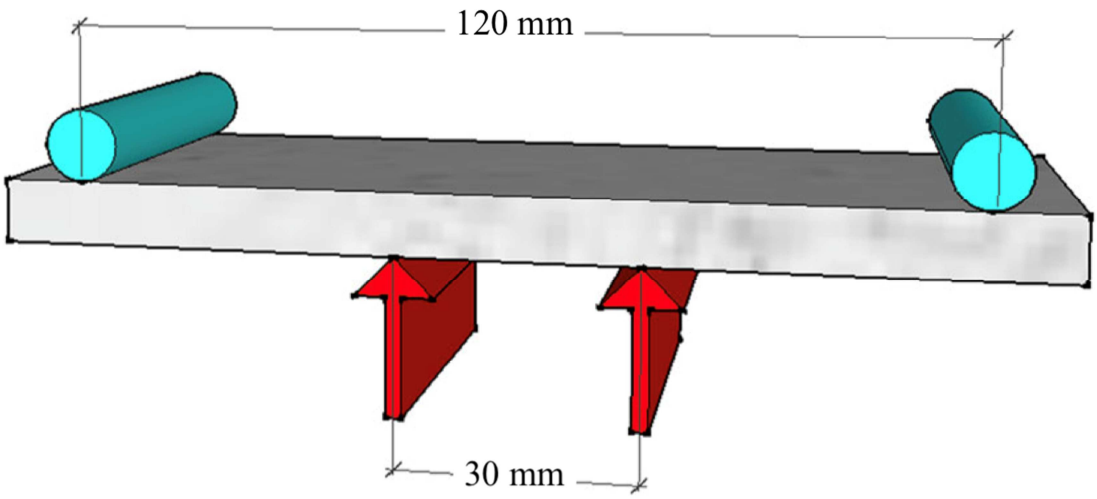

Figure 5. Four-point bending test setup

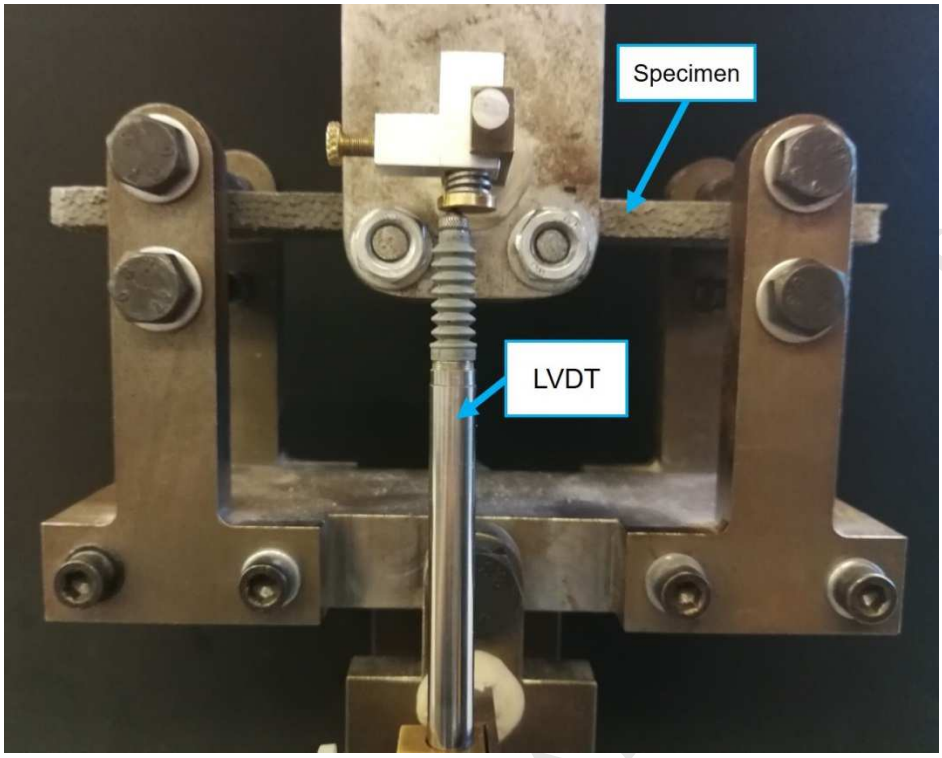

Figure 6. Specimen loaded in four-point bending in the INSTRON 8872

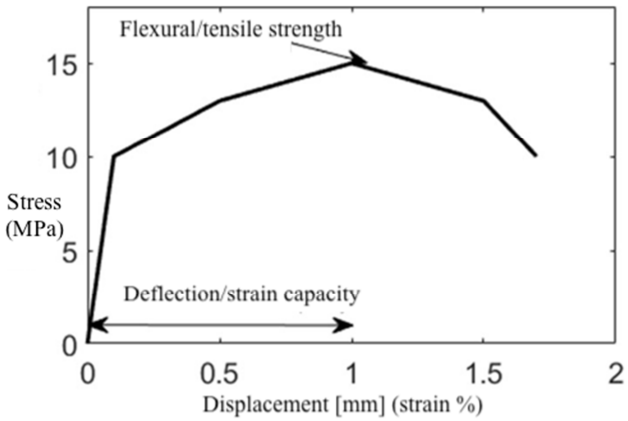

Figure 7. Definition of flexural/tensile strength and flexural deflection capacity/strain capacity as determined by four-point bending/uniaxial tensile tests (adapted from [39])

2.5. Uniaxial tensile test

Similar to the four-point bending tests, uniaxial tensile tests were performed on cured samples using a servo-hydraulic press (INSTRON 8872) under displacement control with a constant rate of 0.005 mm/s. The load was measured by a load cell and the displacements were measured by two linear variable differential transducers (LVDTs) placed on both sides of the specimen. Prior to testing, specimens were glued with a mix of PLEX 7742F and Pleximon on two parallel (non-rotating) steel plates. Specimen size used was 120 x 30 x 8

mm after cutting. The test is shown schematically in Figure 8. For each configuration, three replicate specimens were tested for reference (Ref) and large triangle patterns (LT and LT_R), and four replicate specimens were tested for small triangle patterns (ST and ST_{28}). During the uniaxial tensile test, a camera was placed in front of the specimen to capture photos of the cracking process. Afterwards, digital image correlation (DIC) analyses were performed to determine the strain field on the specimen surface during testing.

In order to obtain input parameters for ABS reinforcement needed for the lattice model, uniaxial tensile tests on printed ABS bars were also performed. The height and width of printed ABS bars was kept constant with the wall of a single cell of printed reinforcement meshes, namely 2 mm in width and 3 mm in height. The length of ABS bars was 100 mm. A same test setup as shown Figure 8 is used. Specimens for four-point bending and uniaxial tension is shown in Figure 9.

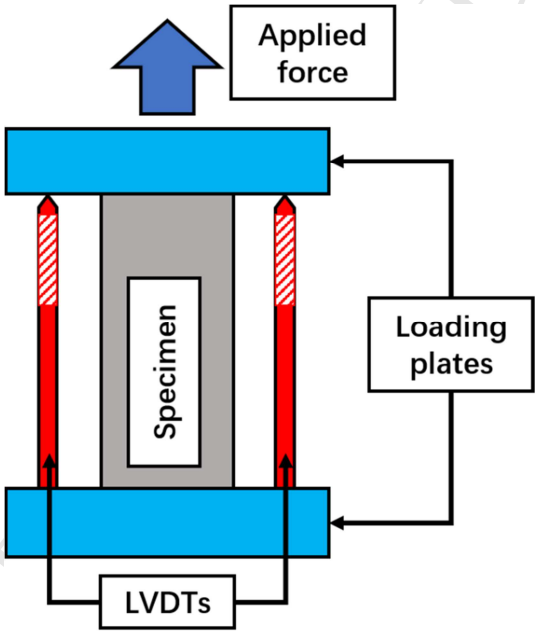

Figure 8. Schematic representation of the uniaxial tensile test on reinforced specimen.

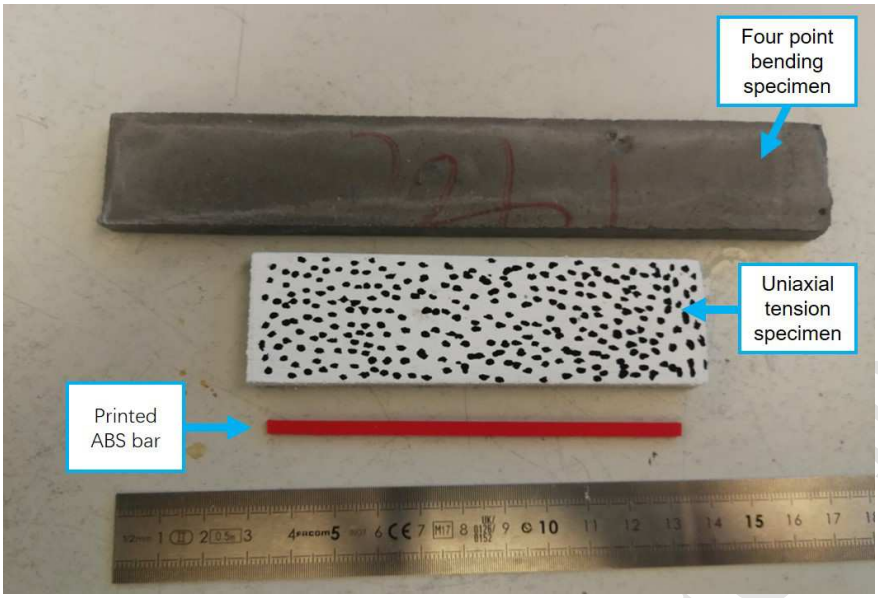

Figure 9 Specimens for four-point bending, uniaxial tension.

2.6. Lattice modeling

Numerical simulations of the deformation and fracture process during four-point bending were carried out using the Delft lattice model. The following modelling procedure was followed:

- A domain with the same size of the specimen (180 mm x 30 mm x 8mm) was generated and divided into a grid of cubic cells with a 1x1x1 mm size.
- A node was generated at a random location in a sub cell of each grid. The ratio of the size of sub cell (s) and grid (A) is defined as the randomness (R=s/A) of the lattice network. In this study R=0.99 is used for all grids (as cementitious material is rather heterogenous, a high randomness is necessary for simulating realistic cracking patterns[40], for all simulated specimen the randomness is kept the same), only the randomness of specimen surface was set to be R=0 in order to apply load and support evenly. The coordinates of a node in the domain were calculated by the following equations.

$$\begin{aligned} x_i &= A*\left((1-R)/2+R*a+i-1\right) \\ y_j &= A*\left((1-R)/2+R*a+j-1\right) \\ z_k &= A*\left((1-R)/2+R*a+k-1\right) \end{aligned} \qquad (1)$$

Where x, y, z is the coordinates of a node locating in the i th grid (integer from 1 to 181) on x axis, j th grid (integer from 1 to 31) on y axis and k th grid (integer from 1 to 9) on z

axis respectively; A is the grid size (see Figure 10); R is randomness ; a is a pseudo random number ranging from 0~1 generated by MATLAB.

- Nodes in adjacent cells were then connected by beam lattice elements forming a heterogenous rectangular lattice network representing the entire domain. In this sense, the heterogeneity of cementitious materials was introduced. Depending on the geometry of reinforced bars and position of the nodes, three categories of lattice elements were generated: matrix elements, interface elements and reinforcement elements. As shown in Figure 10, when an element has two nodes locating in matrix region, it was defined as matrix element and similar criterion applies for defining reinforcement element. When an element has two nodes located in different regions, it was defined as an interface element. The generated lattice networks for the three simulated cases are shown in Figure 11.

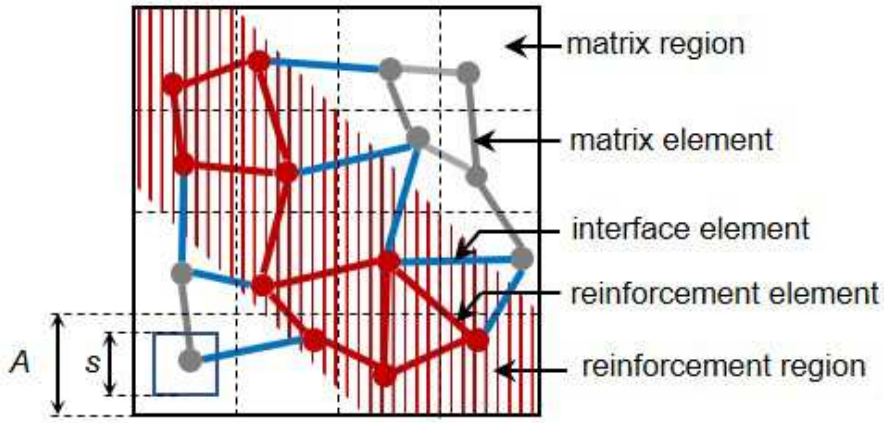

Figure 10. Schematics of domain discretization and element definition (shown in 2D for simplicity)

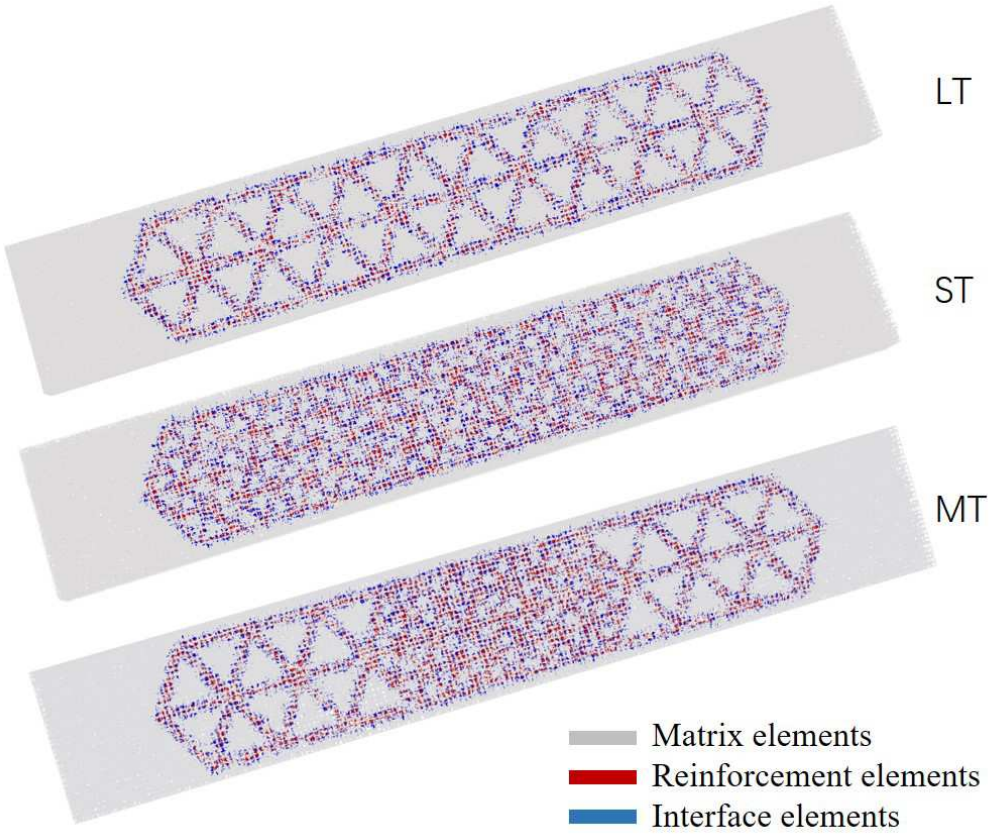

Figure 11 Lattice network of mortar bar reinforced by large triangles and small triangles.

- Linear elastic properties were assigned to the elements according their categories. A prescribed displacement boundary condition was imposed on the lattice network corresponding to the loading boundary condition and a set of linear elastic analyses were performed. In each step, the stress of every element was calculated and one critical element of which the stress exceeded the strength was removed from the lattice. Then, another linear analysis is performed, and this procedure is repeated until the entire lattice system fails. After the computing process, crack pattern and stress-deflection curve were extracted.

In order to obtain input mechanical properties for the lattice elements, several simulations were carried out first to fit reinforcement element properties and matrix element properties using the experiment results on ABS bars and the matrix. The interface element strength was assumed and the elastic modulus was assumed to be the mean value of the Voigt upper bound [40] (calculate by eq.2) and Reuss lower bound (calculate by eq.3) [40] for composites.

$$E_{\mathrm{I}} = V_{\mathrm{m}} E_{\mathrm{m}} + V_{\mathrm{r}} E_{\mathrm{r}} \qquad (2)$$

$$\frac{1}{E_I} = \frac{V_m}{E_m} + \frac{V_r}{E_r} \quad (3)$$

Where E_I, E_m and E_r are the E-modulus of interface element, matrix element and reinforcement element respectively. V_m and V_r are the volume fraction of matrix and reinforcement in an interface element. As the lattice network has rather high randomness (R=0.99), $V_m = V_r = 0.5$ were assumed here for all interface elements.

During the fitting process, input parameters had been varied in the simulation of four-point bending tests on the matrix and uniaxial tensile tests on ABS bars until the simulated results is close to experiment results. The last input parameters were then adopted as inputs for the simulations of reinforced specimens. A comparison of fitting simulation results and experiments are shown in Figure 12, the simulated results are similar to experiment results. The input properties of the simulation are listed in Table 5 . In this work, only four-point bending tests on LT, ST and MT at 7 days were simulated, as in the case of roughed surface much finer grids are required and in tension simulations multiple linear properties as described in [35] are required. Those simulations require too much computational resources, these tests were not simulated here.

Table 5. Input values for lattice model

Element	E-modulus (GPa)	f_t (MPa)	f_c (MPa)
Matrix	14.95	6	-8* f_t
Reinforcement	1.59	35	-2* f_t
Interface	5.57	0.1	-8* f_t

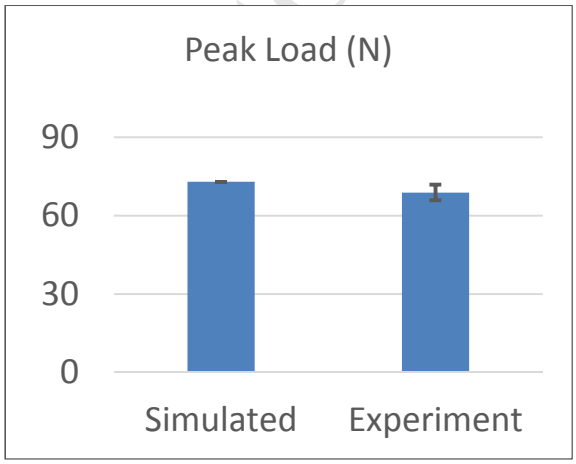

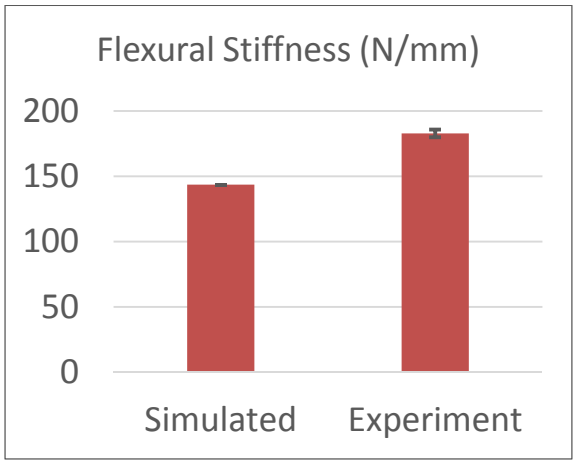

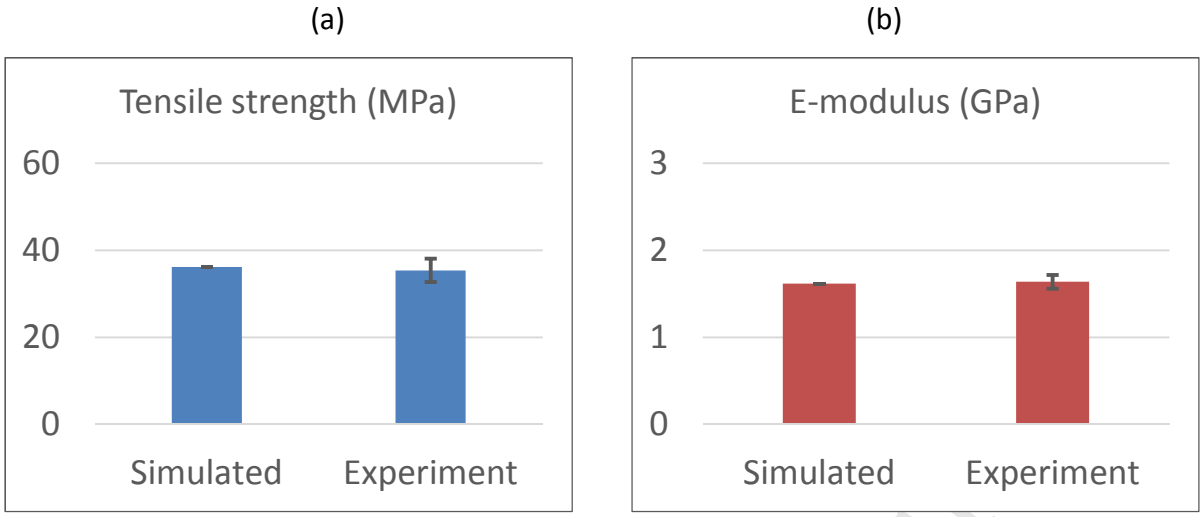

Figure 12 Comparison of simulated values and experiment values of (a) flexural peak load of the matrix, (b) flexural stiffness of the matrix in four-point bending tests, (c) Tensile strength of printed ABS bars, (d) E-modulus of printed ABS bars.

3. Results and discussion

3.1. Four-point bending tests

Flexural stress/deflection curves (average deflection measured by the two LVDTs) for all tested specimens with different 3D printed polymeric reinforcement designs are given in Figure 13 and Figure 14. A summary of the results is given in Table 6.

As expected, at 7d the reference specimens show brittle response with relatively low deflection at failure (Figure 13a). On the other hand, all specimens reinforced with 3D printed polymeric meshes can undertake appreciably higher deformation. Nevertheless, there are significant differences between various reinforcement designs. Not all designs are able to achieve the so-called deflection-hardening behavior, wherein the flexural strength is higher than the first cracking strength. In that sense, looking at the average values given in Table 6 may be misleading in some cases. For the LT pattern, the average flexural strength is higher than the average of the first cracking strength. However, from Figure 13b it is clear that not all LT specimens show deflection hardening behavior. In fact, only specimen LT 1 (shown in blue) shows deflection hardening behavior. In other specimens, although they do not fail after the first crack occurs, the stress does not exceed the first cracking strength. In essence, although large triangular reinforcement does provide these specimens with some ductility, it cannot be used for obtaining (reliable) deflection hardening. In cementitious materials such as e.g. SHCC, deflection hardening is typically achieved through multiple cracking. Multiple cracking (witnessed by large drops in the stress/deflection diagrams) was

not observed in LT series, which mostly had only two cracks, typically close to the loading points (as shown in Figure 15). The ductility in this case was provided by the pullout of the polymeric reinforcement from the cementitious matrix. Note that a different matrix design could possibly result in deflection hardening even in this case, e.g. if a weaker matrix would have been used. This will be studied in the future.

All specimens from other series showed a characteristic deflection hardening behavior. First, the 7d ST series (Figure 13c) showed deflection hardening achieved through multiple micro-cracking. Compared with the LT series, this is clearly an improvement. This was expected, however: similar to conventional fiber reinforced cementitious composites, more ductility is achieved with a higher percentage of fiber reinforcement. It is very interesting to note, however, as shown in Figure 13d that the MT (i.e. "functionally graded") series showed deflection hardening behavior as well, achieved through multiple micro-cracking (multiple cracks can be found in Figure 15). Again, in this series, the designed polymeric mesh was denser in the middle (constant moment region) than at the sides. This simple modification shows great potential of additive manufacturing: it is possible to achieve significant savings in the material if the reinforcement design is such that it is used only where needed (i.e. regions of high stress). This is something that cannot be achieved by conventional fiber reinforcement. The design with additively manufactured surface roughness (MT_R) did not show markedly different behavior (Figure 13e) – deflection hardening was achieved in this case as well. It is possible that, if the cementitious matrix would have been weaker, surface roughness would have had a higher impact on the post-peak behavior. This will be further studied in the future.

The two series at 28d of small triangles (ST_{28}) and mixed triangles (MT_{28}) were also tested, flexural stress-deflection curves are shown in Figure 14 . Normally, mortar bars with longer curing age are stronger and more brittle. This can also be found in Table 6 , the flexural strength of 28d specimen are higher and the strain capacity is lower. It could be even more difficult to have deflection hardening behavior for the reinforced mortar bars. However, as can be seen in Figure 14b and Figure 14c , both ST_{28} series and MT_{28} series still showed obvious deflection hardening behavior.

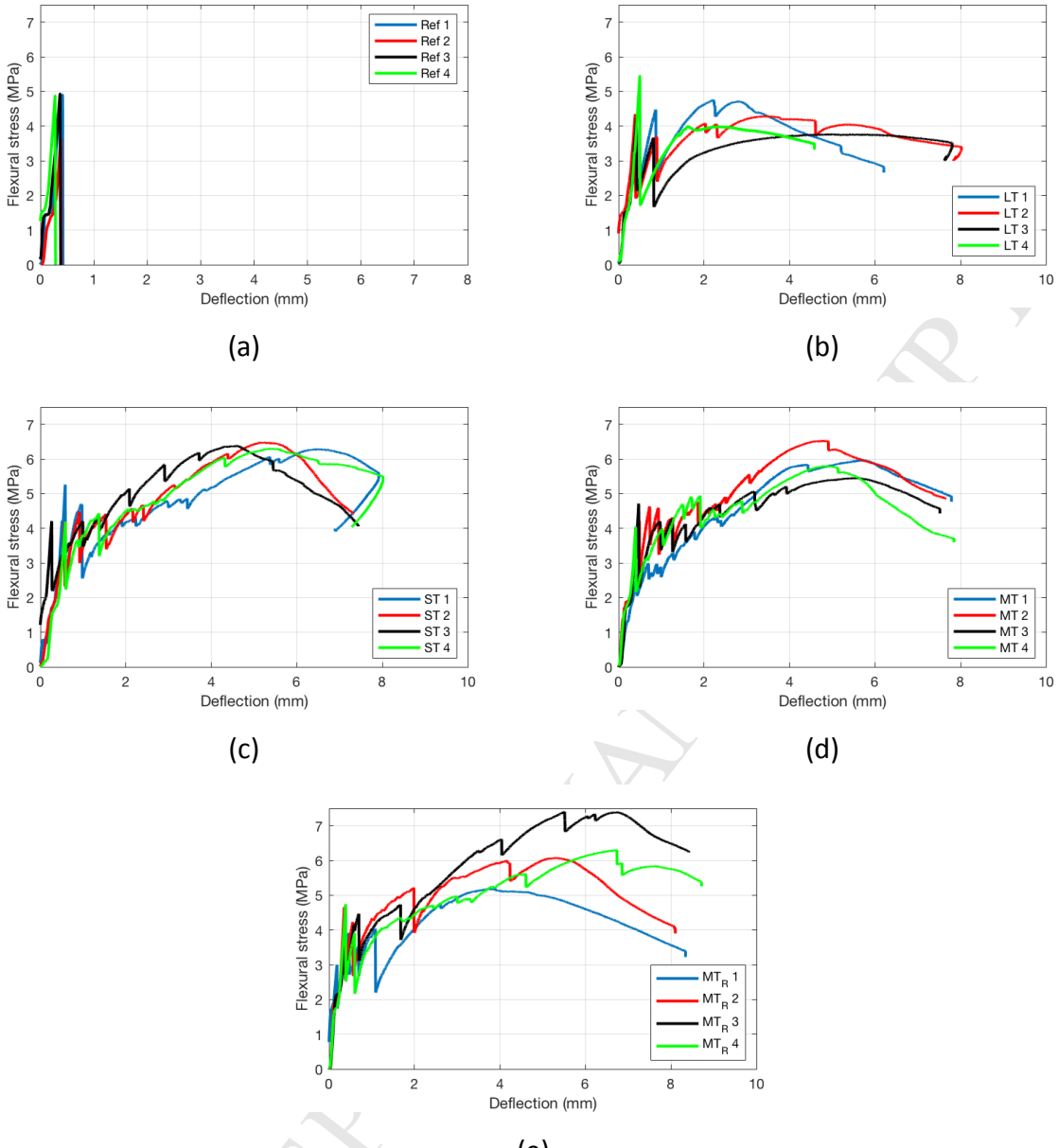

Figure 13. Flexural stress-deflection curves for7d specimens tested in bending. (a) reference (no reinforcement); (b) large triangles (LT); (c) small triangles (ST); (d) mixed triangles (MT); (e) mixed triangles with a rough surface (MT_R).

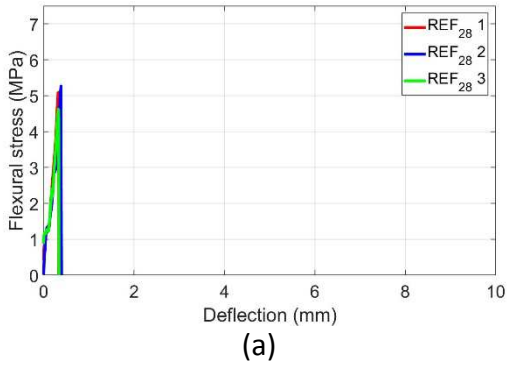

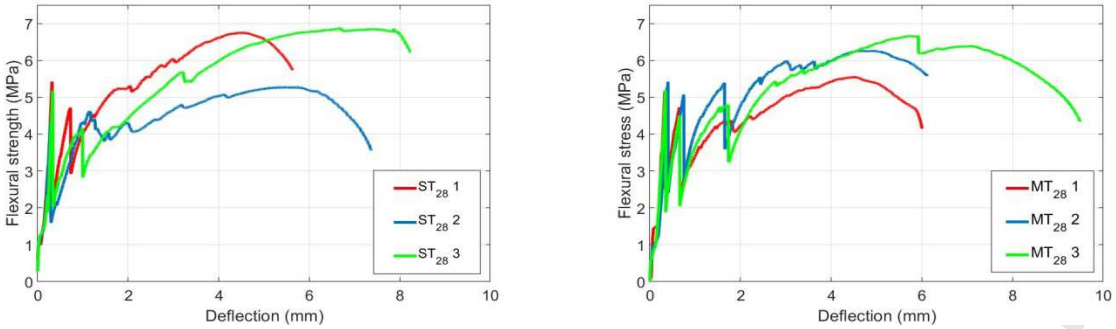

Figure 14 Flexural stress-deflection curves for 28d specimens tested in 4-point bending. (a) reference (no reinforcement); (b) small triangles (ST_{28}); (c) mixed triangles (MT_{28}).

Table 6. A summary of four-point bending results

Series	*First cracking strength (Standard deviation) [MPa]*	*Flexural strength (Standard deviation) [MPa]*	*Deflection capacity (standard deviation) [mm]*
Ref	4.584 (0.549)	4.584 (0.549)	0.361 (0.052)
LT	4.514 (0.546)	4.693 (0.472)	0.944 (0.881)
ST	4.308 (0.606)	6.127 (0.337)	5.429 (0.675)
MT	4.321 (0.666)	6.002 (0.541)	5.312 (0.605)
MT_R	4.255 (0.712)	6.243 (0.784)	5.369 (1.010)
Ref_{28}	4.992 (0.337)	4.992 (0.337)	0.343 (0.036)
ST_{28}	4.973 (0.583)	6.298 (0.890)	5.545 (1.012)
MT_{28}	5.255 (0.147)	6.162 (0.569)	4.985 (0.661)

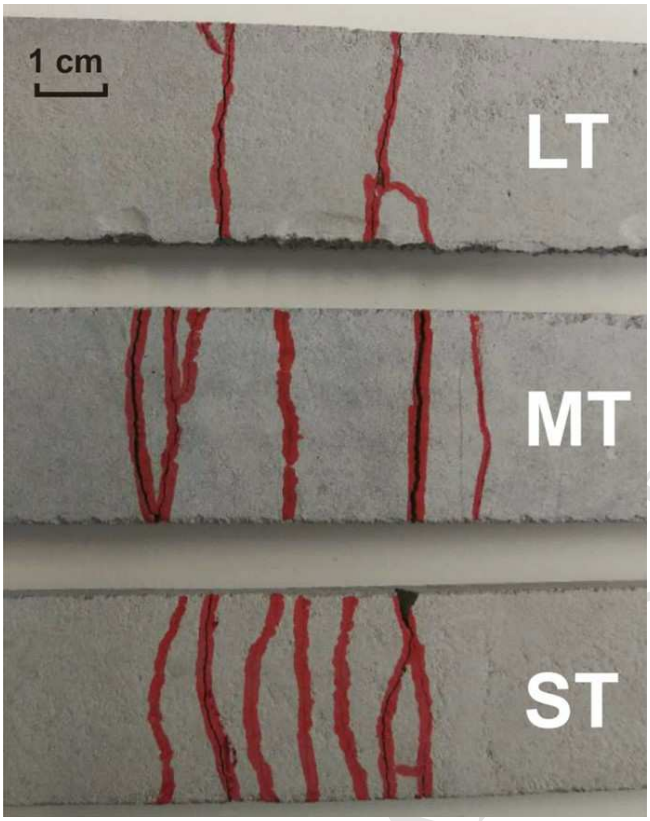

Figure 15 Highlighted cracks in the middle region of specimens with larger triangles (LT), mixed triangles (MT) and small triangles (ST), respectively, after the four-point bending test.

In Figure 16-Figure 17, the reinforced specimens and reference specimens are compared in terms of the first cracking strength, flexural strength, and deflection capacity for different specimen series. From Figure 16, it can be seen that the first cracking strength is not obviously affected when printed mesh is used in all experimental series of the same age. The highest difference between the reinforced specimens and reference is 7.2% (between Ref and MT_R) at 7d and 5.3% (between Ref_{28} and MT_{28}) at 28d. However, while the LT series doesn't show an obvious increase in average flexural strength compared to the reference (increase is less than 2.5%), other series show a significantly increased flexural strength (33.7%, 30.9% and 36.2% for the ST, MT, and MT_R series, respectively). Similar increase in flexural strength at 28d can also be found: 26.2% and 23.4% for ST_{28} and MT_{28} respectively. The increase in the flexural strength is a result of deflection hardening in these series. The most important difference between different series is the flexural deflection capacity (Figure 17). While the LT specimen series shows only a slightly higher average flexural deflection capacity compared to the reference (and only due to the one specimen which did exhibit deflection hardening), other tested series ST, MT, MT_R, ST_{28} and MT_{28} all show significantly improved flexural deflection capacity. It is rather interesting that at 7d and 28d, small triangle series

(ST and ST_{28}) and mixed series (MT, MT_R and MT_{28}) show quite similar increased flexural deflection capacity comparing to reference: at 7d, 1403% (ST), 1345% (MT) and 1387% (MT_R). At 28d, they are 1516% (ST_{28}) and 1353% (MT_{28}). This is an additional proof that, with additive manufacturing of reinforcement, there is potential for creating functionally graded cementitious composites and thereby optimizing material usage. Additionally, MT_R and MT have quite similar flexural strength and deflection capacity. Comparing to flat surface designs, the rough surface design did not provide the reinforced mortar bars with any additional ductility in the performed tests.

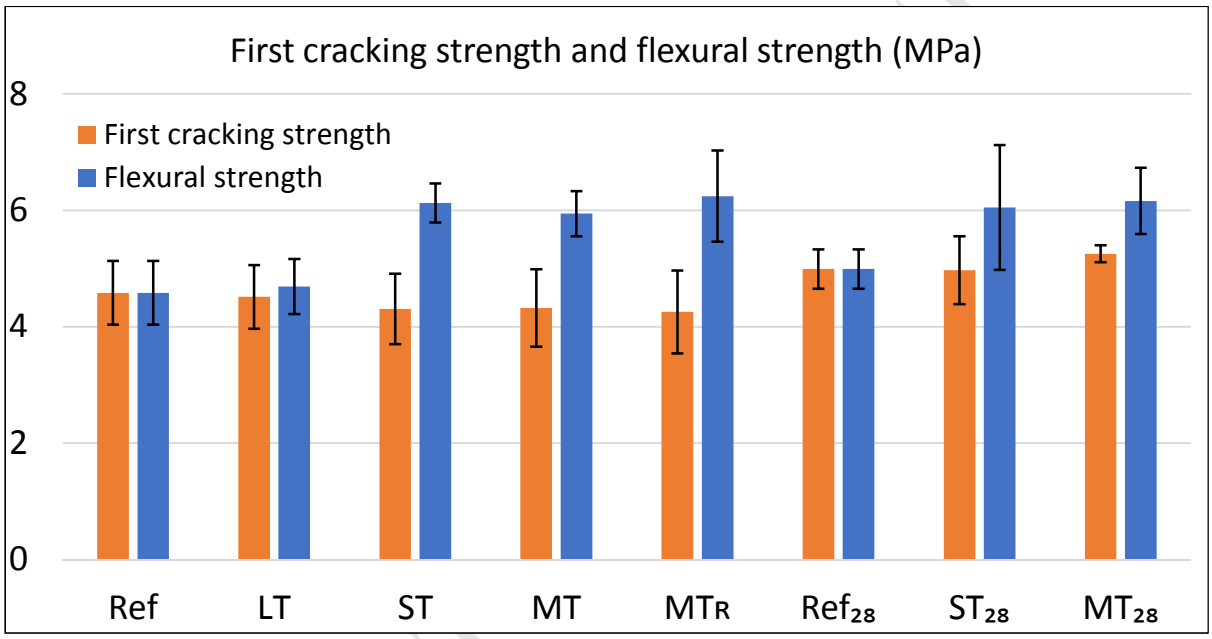

Figure 16. Comparison of first cracking strength and flexural strength of specimens tested in four-point bending (standard deviation is indicated).

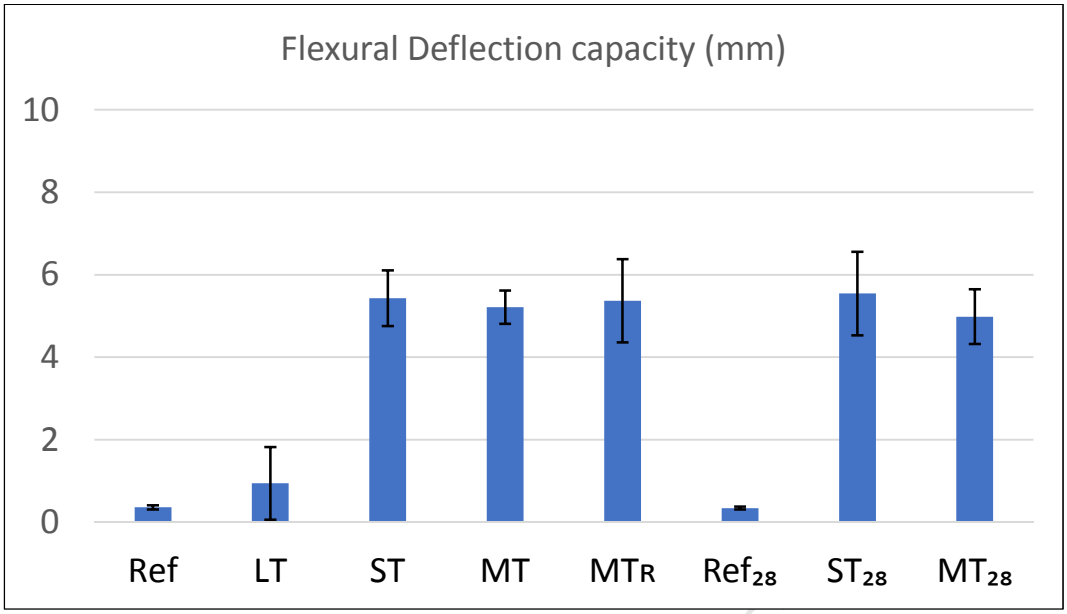

Figure 17. Flexural deflection capacity of specimens tested in four-point bending (standard deviation is indicated).

Correspondingly, as can be seen in Figure 18, the simulated curves of LT and ST both show good agreement with experiments. For LT (shown in Figure 18a), after the first peak the reinforcement took over the load and stress increased again while the stress is always lower than the first peak until the specimen failed, deflection hardening behavior was not achieved. Although ductility of the specimen was increased from the simulated flexural stress-deflection curve, only two main cracks can be seen from the fractured specimen (shown in Figure 19a), which resembles the cracking pattern obtained from the experiment (Figure 15). For ST and MT, the simulated stress-deflection also corresponds to the experiment (shown in Figure 18b and Figure 18c). After the first crack, the stress increased and was higher than the first peak until failure. Multiple cracking behavior can be observed from the cracking history (shown in Figure 19b and Figure 19c).

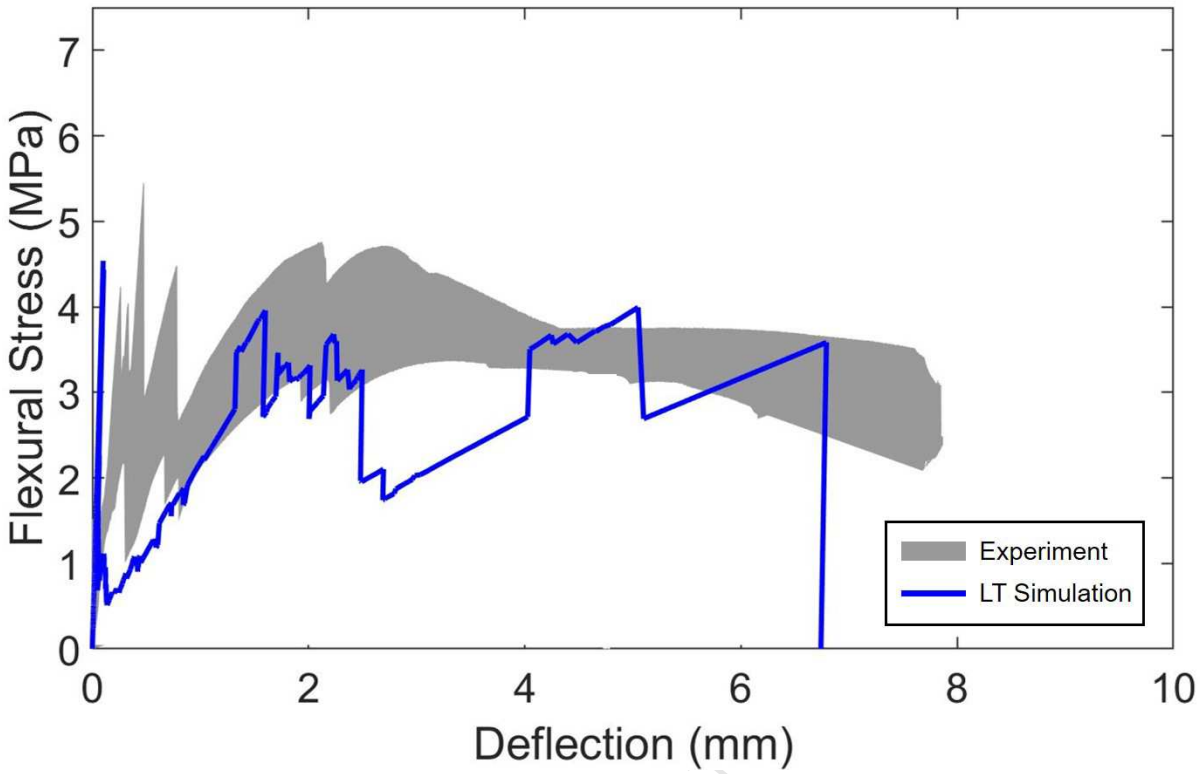

407

408 (a)

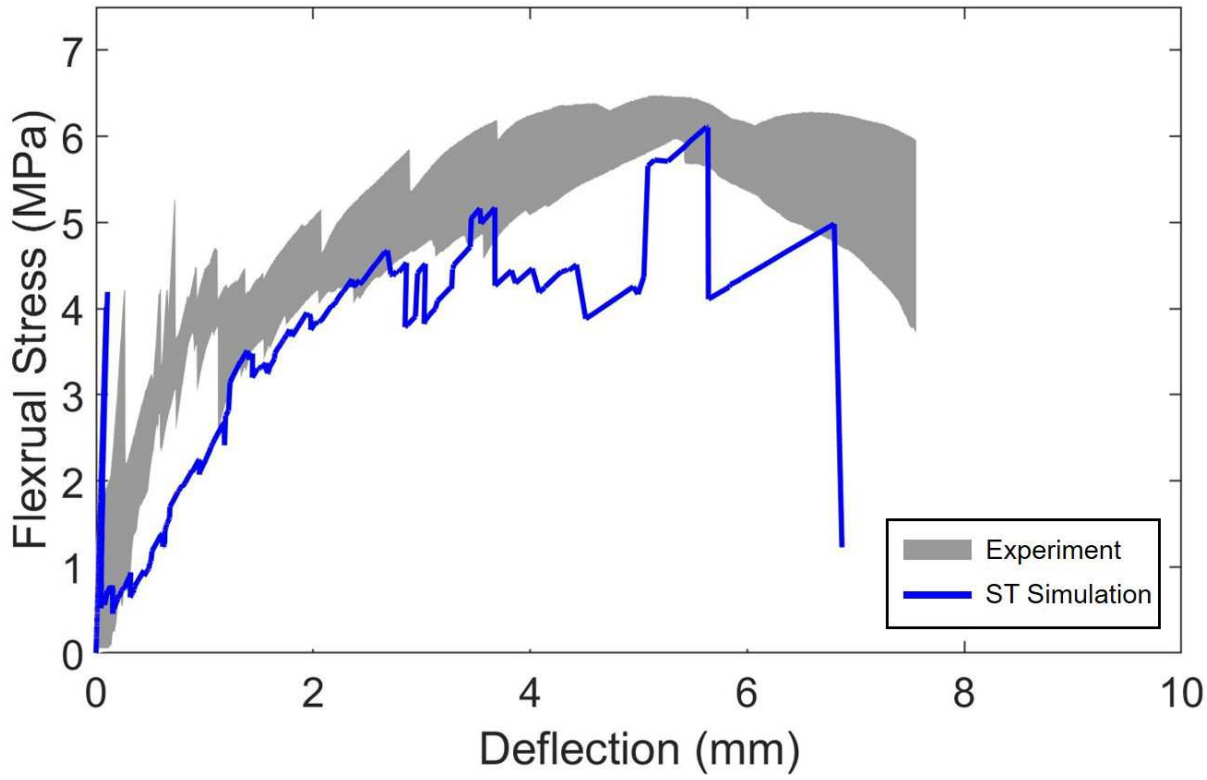

409

410 (b)

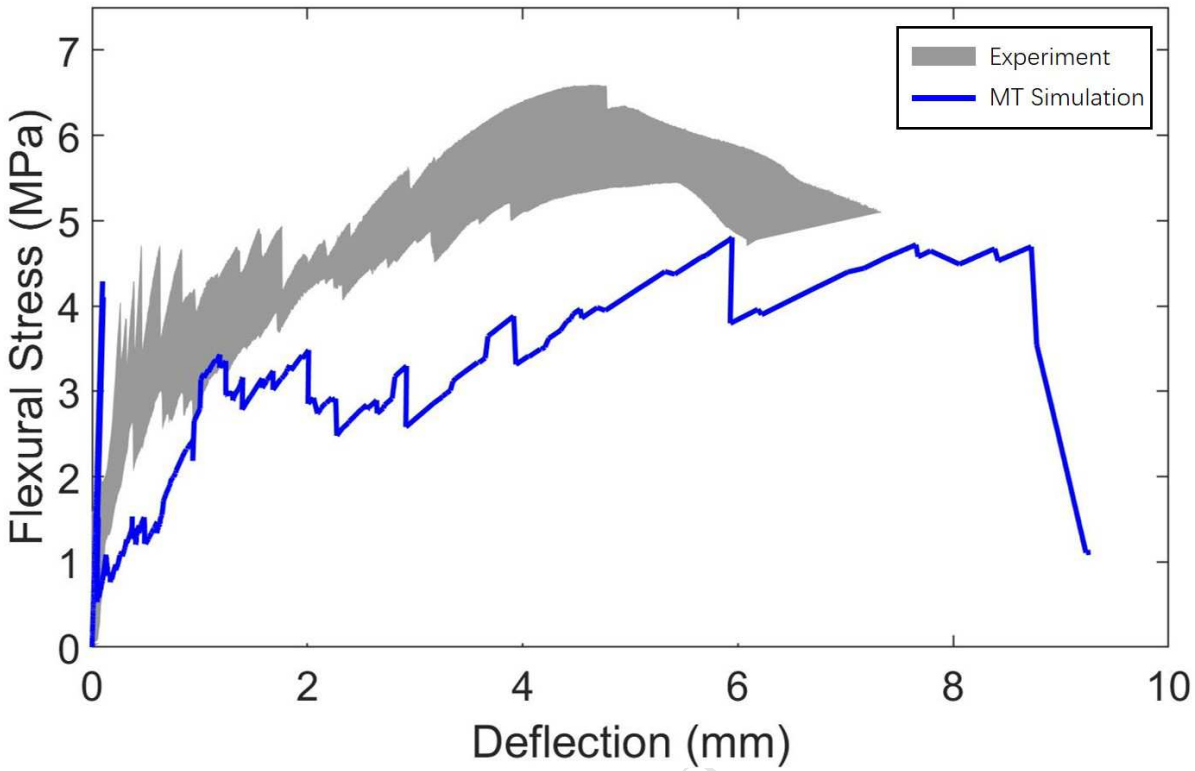

(c)

Figure 18 Comparison of experiment results and simulation results of four-point bending tests on mortar bars reinforced by (a)large triangles and (b)small triangles.

(a)

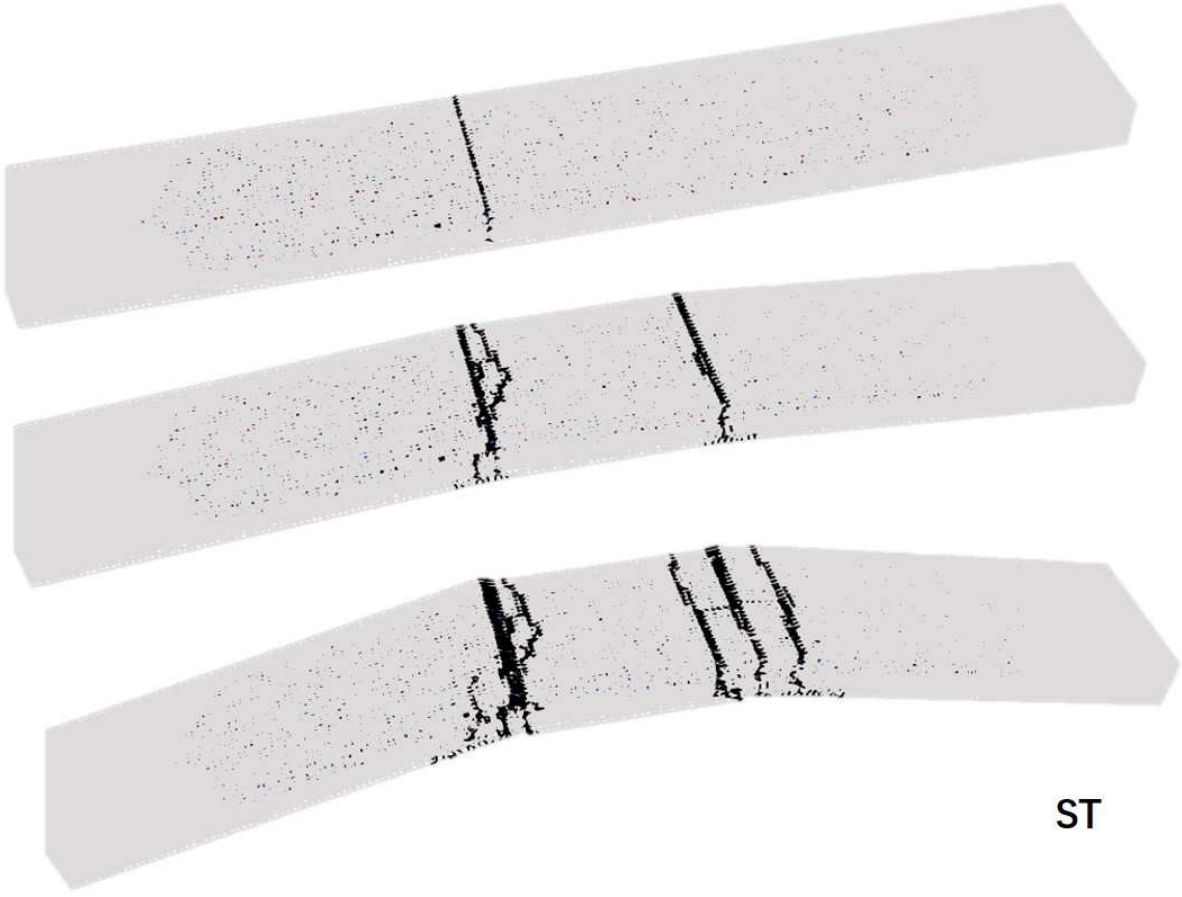

(b)

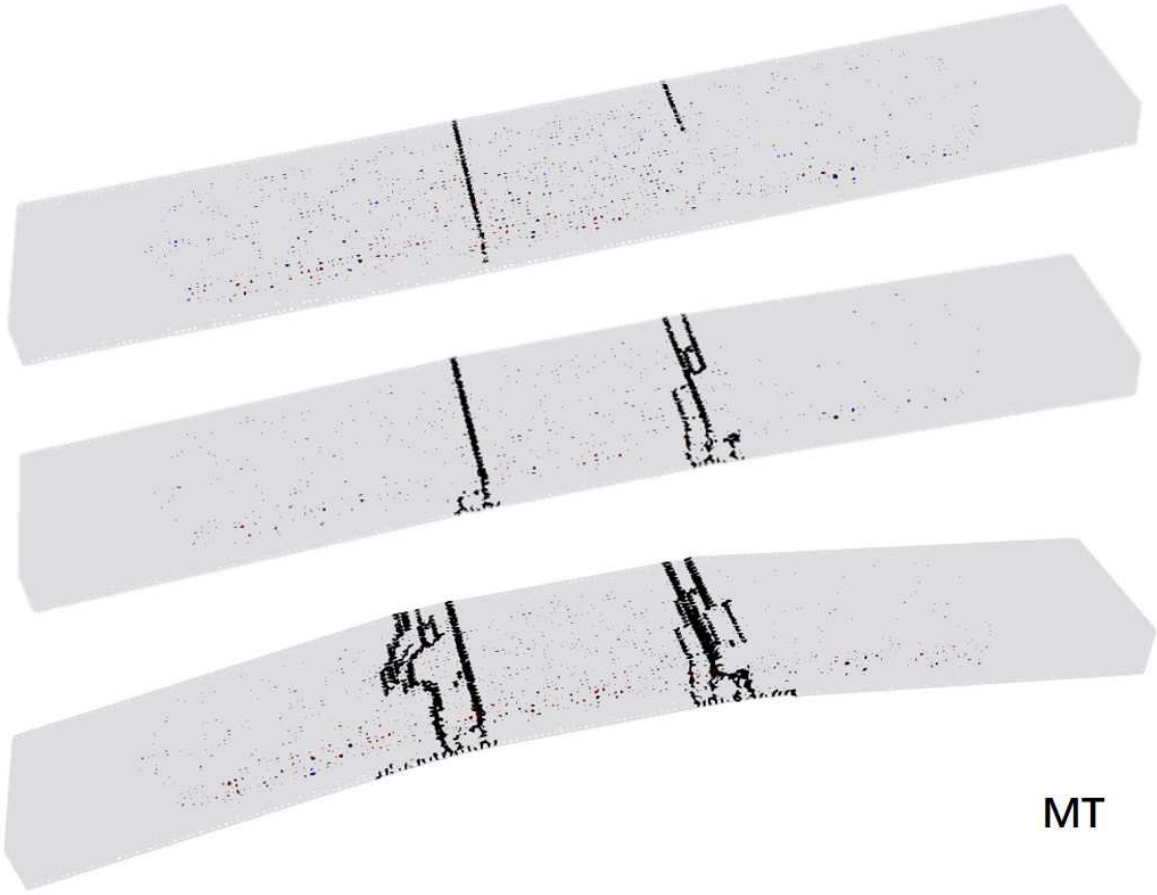

(c)

Figure 19 Simulated cracking history of (a) 7d large triangles, (b) 7d small triangles (ST) and (c) 7d mixed triangles (MT), black elements are failed elements.

3.2. Uniaxial tension tests

Uniaxial stress/strain curves (average strain measured by the two LVDTs) for all tested specimens reinforced by 3D printed polymeric meshes with different patterns are given in Figure 20. A summary of the results is given in Table 7. It is clear that the reference specimen (i.e. the one without polymeric reinforcement) exhibits brittle behavior in tension (Figure 20a), which is typical of cementitious materials [41]. It has a low strain capacity and only a single crack formed. On the other hand, all specimens reinforced with 3D printed polymeric meshes are capable of undertaking larger strains. Furthermore, as can be seen from Figure 20, in tension all tested reinforced specimens of various configurations did show strain hardening behavior: after the first cracking, all reinforced specimens were able to carry increasing amounts of stress until the maximum stress was reached. Still, different behaviors of reinforced specimens are obvious within varied reinforcement patterns.

The large triangle patterns (LT and LT_R) exhibit quite similar strain hardening behavior: after cracking, only a few cracks formed before the ultimate strain was reached. The stain

hardening behavior occurred mainly not from multiple cracking mechanism but the so called slip hardening behavior [35] - namely the friction between the reinforcement and the matrix which resists the slippage. In the observed case, the friction is sufficient to result in slip hardening behavior, providing the LT_R and LT with overall higher strain capacity. As the roughed surface provides higher friction (rough surface has more contacting area between matrix and reinforcement), the strain capacity of LT_R series (0.741%) is slightly higher than LT series (0.503%).

Comparing to the large triangle patterns, the multiple cracking behavior of specimens reinforced with small triangles (ST and ST_{28} series) is much more obvious which is similar to the typical strain hardening behavior of e.g. SHCC [17, 18] or TRC [24, 25]. In most specimens in ST and ST_{28} series, numerous drops in the stress-strain curve indicate multiple cracks forming in the loading process. Finally, after the maximum stress is reached, the specimen fails in a similar manner to LT specimens, i.e. through pullout of the polymeric reinforcement and localization of a single wide crack. It is interesting to observe that in ST series (Figure 20), results of all specimens are quite constant, only in the final pulling out stage, two specimens (ST 2 and ST 4) behave differently than other specimens in the final pull out stage: instead of being pulled out at the final drop, the printed meshes were suddenly ruptured in tension (sudden drop of the last peak) which resulted in relatively higher strain capacity and flexural strength.

In previous section, the flexural strength of 28d reference specimens are slightly stronger than 7d reference specimens. However, in tension the influence of curing age on the tensile strength of the matrix is considerable. From Table 7, tensile strength of the reference series at 28d (3.444 MPa) is much higher than that of reference series at 7d (1.705 MPa) and consequently, the stain capacity of ST_{28} series (0.579%) is much lower than ST series (1.135%).

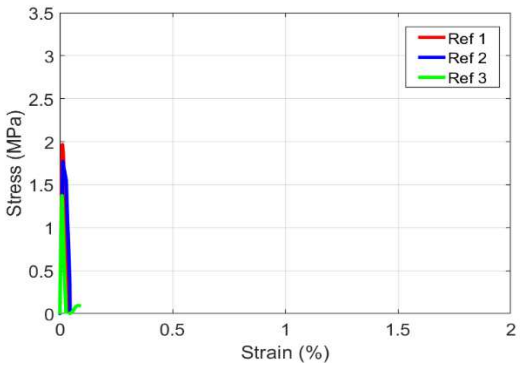
Ref 1
Ref 2
Ref 3
Stress (MPa)
Strain (%)

(a)

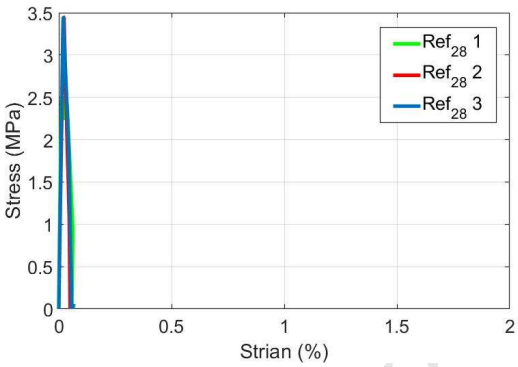
Ref28 1
Ref28 2
Ref28 3
Stress (MPa)
Strian (%)

(b)

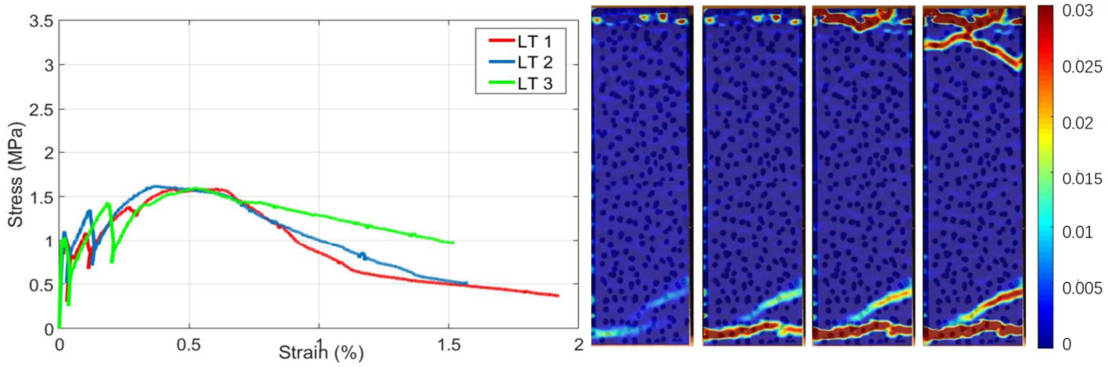
LT 1
LT 2
LT 3
Stress (MPa)
Strain (%)

(c)

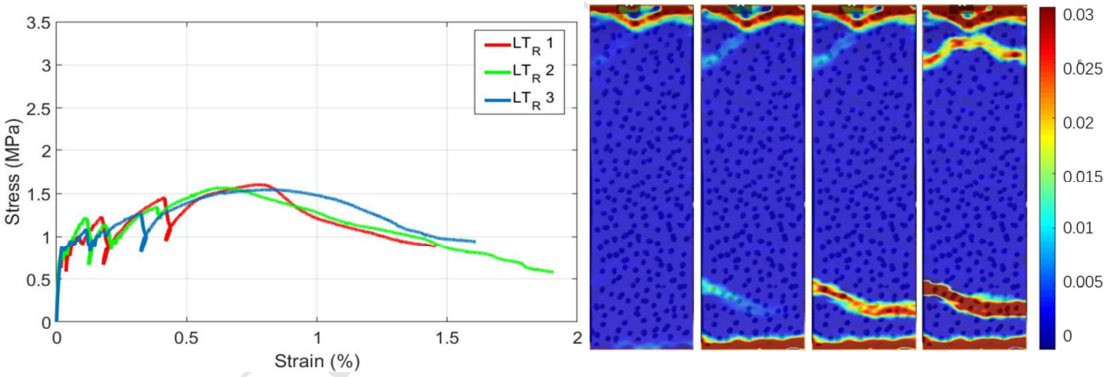
LTR 1
LTR 2
LTR 3
Stress (MPa)
Strain (%)

(d)

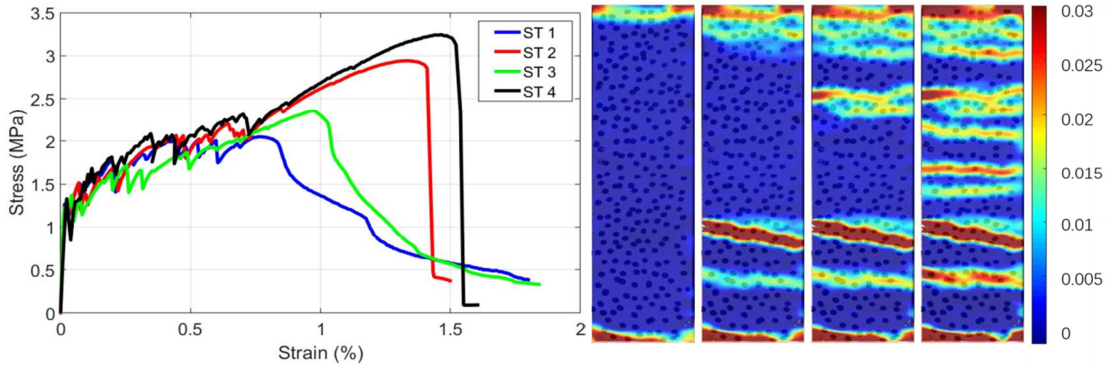
ST 1
ST 2
ST 3
ST 4
Stress (MPa)
Strain (%)

(e)

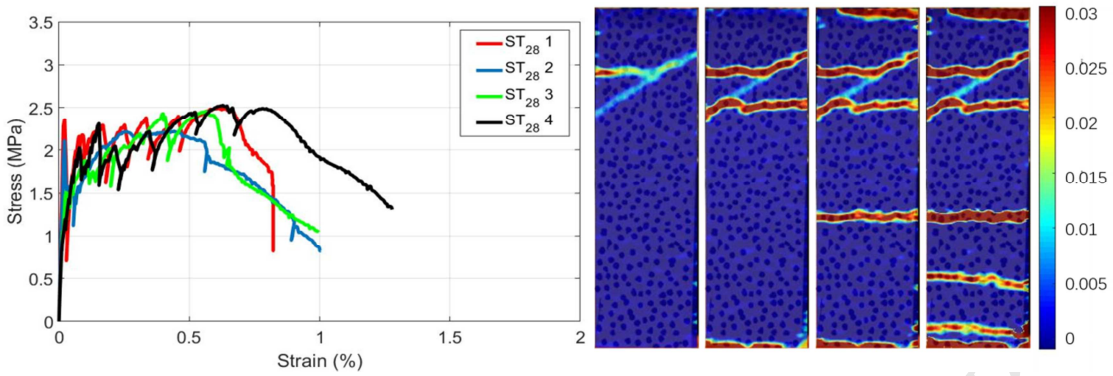

(f)

Figure 20. Tensile stress-strain curves and corresponding DIC results for specimens reinforced with different 3D printed polymeric meshes. (a) reference (no reinforcement) at 7d; (b) reference (no reinforcement) at 28d; (c) large triangles at 7d (LT); (d) large triangles with a rough surface at 7d (LT_R); (e) small triangles at 7d (ST); (f) small triangles at 28d (ST_{28}).

Table 7. A summary of uniaxial tension results

Series	*First cracking strength (Standard deviation) [MPa]*	*Tensile strength (Standard deviation) [MPa]*	*Strain capacity (standard deviation) [%]*
Ref	1.705 (0.302)	1.705 (0.302)	0.012 (0.002)
LT	0.944 (0.051)	1.604 (0.017)	0.503 (0.120)
LT_R	0.784 (0.087)	1.572 (0.030)	0.741 (0.111)
ST	1.223 (0.070)	2.647 (0.543)	1.135 (0.323)
Ref-28d	3.136 (0.533)	3.136 (0.533)	0.021 (0.002)
ST-28d	1.093 (0.181)	2.424 (0.140)	0.579 (0.095)

Figure 21 provides a comparison between correlated first cracking strength (first cracking strength divided by cross sectional reinforcing ratio) and tensile strength of different series. As can be seen in Figure 21, all reinforced specimens show significant improvement compared to the first cracking strength which is a result of strain hardening in these materials. In uniaxial tension tests, because part of the cross section is replaced by the printed mesh in reinforced specimen, the real cross section area of the matrix is smaller than that of the reference specimen, which resulted in lower calculated first cracking strength in reinforced series. In this sense, the matrix cracking strength is correlated according to the

first cracking strength and the highest cross-sectional reinforcing ratio from Table 3 of each pattern. As shown in Figure 22, considering the deviation, there is no significant difference between the reinforced test series and reference specimens in correlated cracking strength of the matrix. Still, in LT series the correlated first cracking strength is relatively lower. This could be the fact that printed reinforcement might introduce many interfacial zones between the matrix and the reinforcement making the crack easier to initiate in the reinforced specimens. Furthermore, matrix compaction is somewhat more difficult in the reinforced series due to the spacing regions of the printed reinforcement, possibly causing more imperfections to form in some of the specimens compared to the reference series.

Even more significant improvements can be seen in terms of tensile strain capacity (Figure 23): the tensile strain capacity is increased by 4540%, 6750%, and 6600% compared to the reference series the LT, ST and LT_R series, respectively. Even with a simple reinforcement mesh design used in this preliminary work, these are significant improvements. Clearly, there is still room for improvement. This indicates a huge potential that additive manufacturing has in creating strain hardening cementitious composites.

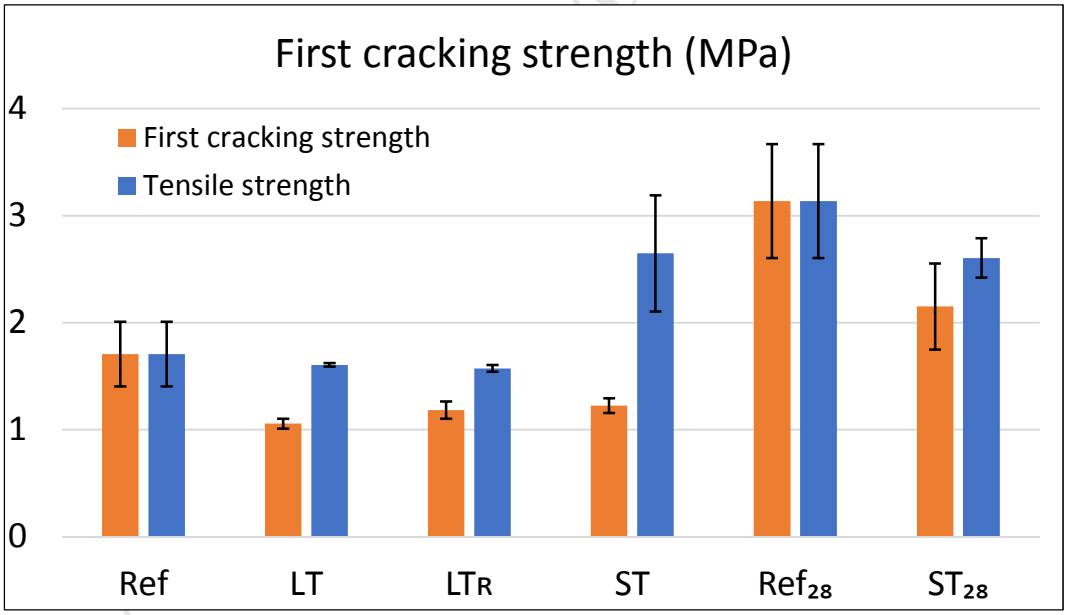

Figure 21. First cracking strength and Tensile strength of specimens tested in tension (standard deviation is indicated).

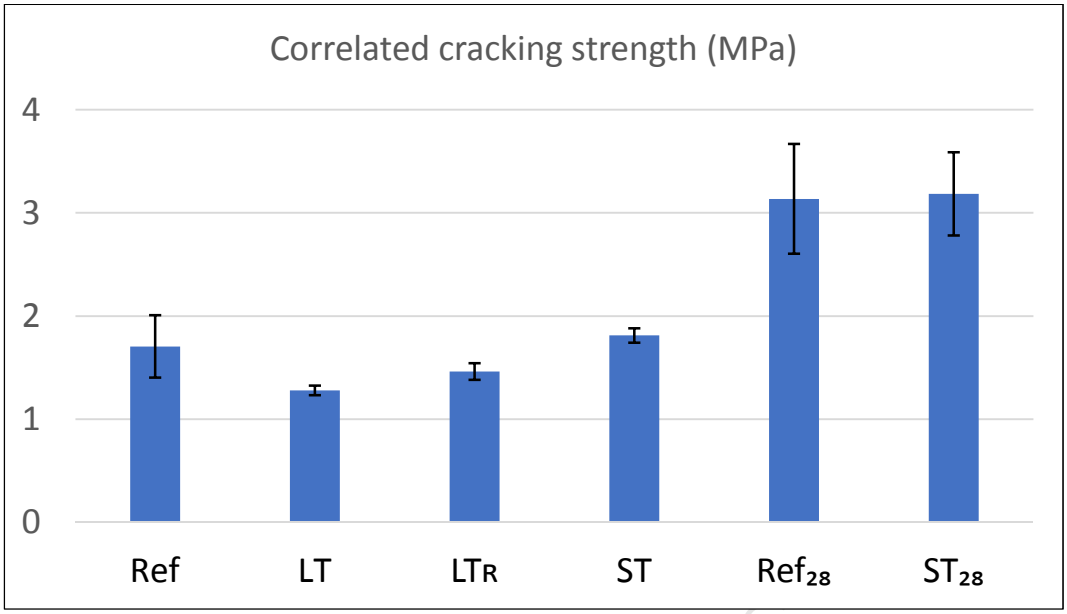

Figure 22 Correlated cracking strength of the matrix (standard deviation is indicated)

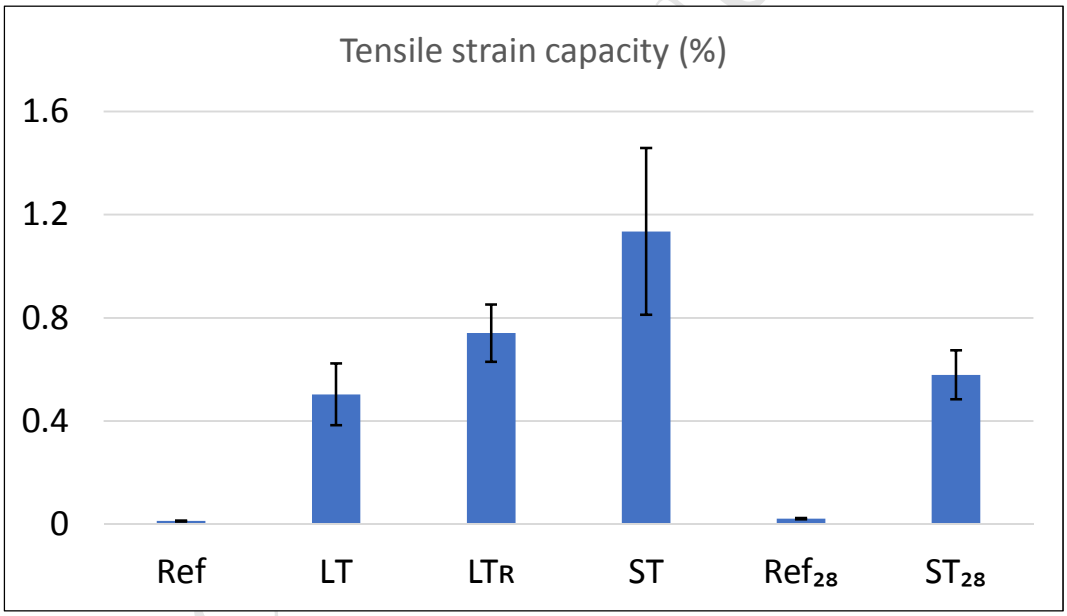

Figure 23. Tensile strain capacity of specimens tested in tension (standard deviation is indicated).

4. Conclusions

In this work, a preliminary study of using additively manufactured polymeric meshes as reinforcement for creating strain hardening cementitious composites. Simple reinforcement meshes were designed, manufactured, and tested in four-point bending and uniaxial tension. In addition, four-point bending tests were simulated using the lattice model. Based on the performed experiments and simulations, the following conclusions can be drawn:

- Certain designs of 3D printed polymeric meshes enable creating composites with strain hardening and deflection hardening behavior. This mainly depends on the mesh design in terms of a same matrix.
- Use of 3D printed polymeric reinforcement enables significantly increasing the deflection and tensile strain capacity of cementitious composites compared to the reference material.
- According to experimental results, deflection hardening was observed only in specimens which showed multiple cracking. Other specimens (in which pullout of the reinforcement was the only mechanism) did show increased ductility compared to the reference, but no significant hardening was observed.
- Numerical simulation results show good agreement with the experiment, specimen reinforced by finer mesh (ST) and mixed mesh (MT) show multiple cracking behavior and deflection hardening was obtained while specimen reinforced by coarser mesh (LT) didn't show multiple cracking and deflection hardening.
- Strain hardening was observed in all designs of polymeric reinforcement tested. Unlike the case of bending, this is valid for both those exhibiting multiple cracking and those wherein reinforcement slip is the main mechanism observed.
- In four-point bending, a simple mesh pattern (MT) showed great potential of using additive manufacturing for creating functionally graded cementitious composites.
- Surface roughness designed and created by the additive manufacturing process can be used as an additional option for creating strain hardening cementitious composites by manipulating the bond between the polymeric mesh and the cementitious matrix.

Although this research shows great potential of the proposed approach, there are still many issues that need to be studied. First, in this research, the focus was on the mesh design, while the cementitious matrix was kept constant. It should be noted, however, that the behavior of the composite does not depend only on the design of the reinforcement, but also on the matrix properties [42]. In this research, a matrix with rather low w/b ratio (0.33, Table 1) was used, resulting in a relatively strong material after 28 days. It is possible that even higher deflection and strain capacity could be obtained with lower w/b ratio. Furthermore, no detailed knowledge of the bond behavior between the 3D printed polymeric

reinforcement and the cementitious matrix is available at present. In this research, this parameter has been changed only by manipulating the physical bond through creating surface roughness in some cases. Other possible treatments, such as e.g. coating of reinforcement to improve the chemical bond, have not been studied. This will be a part of future research. Finally, printing parameters of 3D printing were kept constant in this research. These parameters may significantly influence the properties of the printed reinforcement. This also needs to be investigated further in the future.

Acknowledgements

Yading Xu would like to acknowledge the funding supported by China Scholarship Council (CSC) under the grant CSC No.201708110187. The authors would like to acknowledge Mr. Vincent Huigen, Mr. Jorgi Penners and Mr. Bas Berger for their help in the sample preparing and mechanical tests.

Appendix

Load-Deflection curves of 7 days four-point bending tests are shown in Figure A.1.

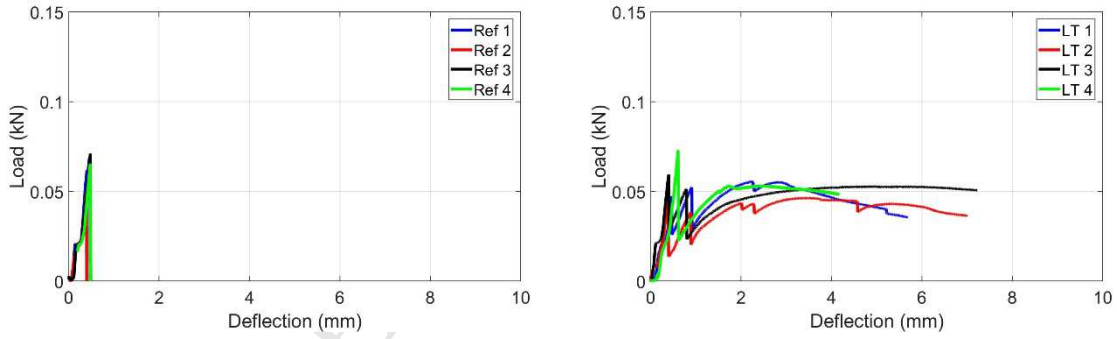

(a) (b)

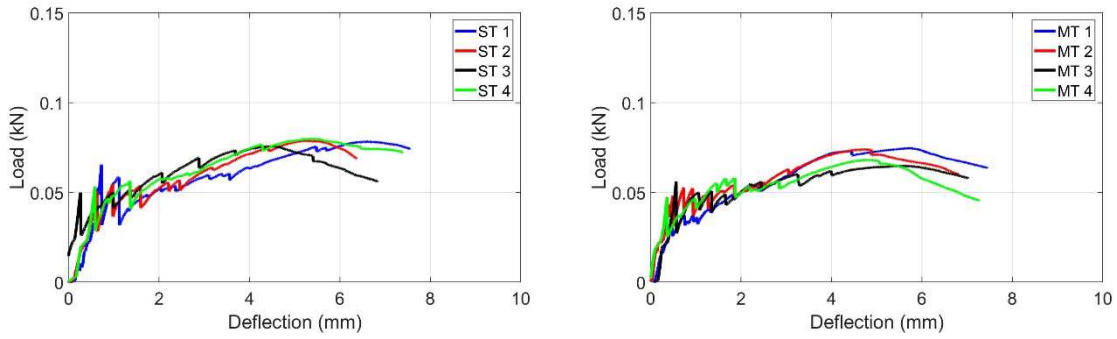

(b) (d)

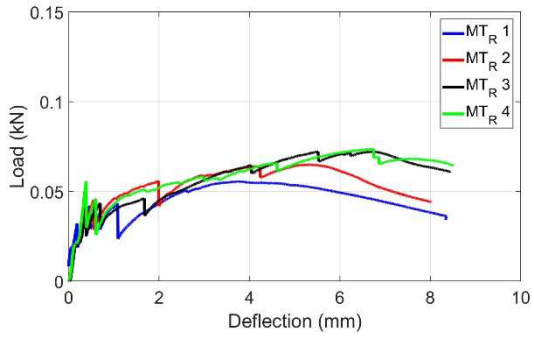

(e)

Figure A.1 Load-deflection curves of 7 days specimen. (a) reference (no reinforcement); (b) large triangles (LT); (c) small triangles (ST); (d) mixed triangles (MT); (e) mixed triangles with a rough surface (MTR).

Load-Deflection curves of 28 days four-point bending tests are shown in Figure A.2.

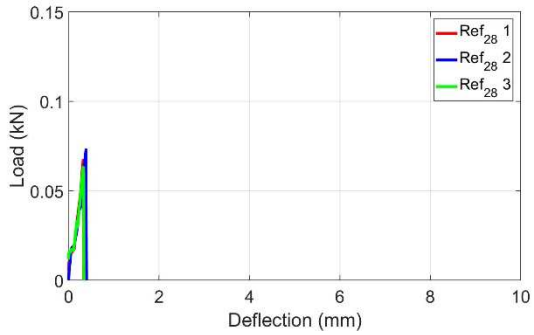

(a)

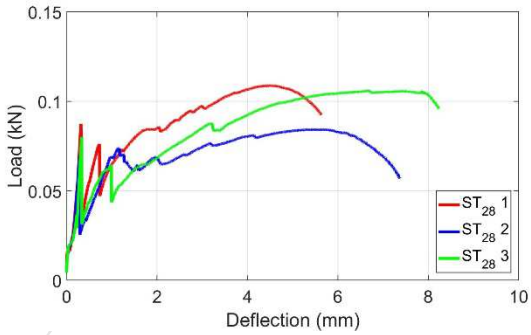

(b)

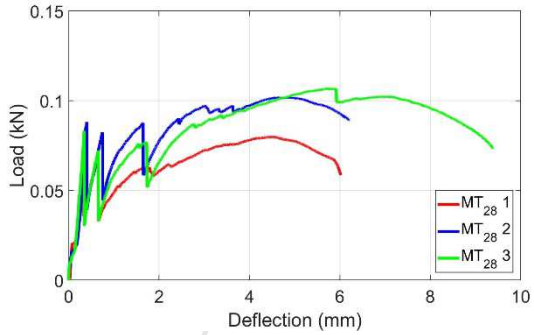

(c)

Figure A.2 Load-deflection curves for 28d specimens tested in 4-point bending. (a) reference (no reinforcement); (b) small triangles (ST_{28}); (c) mixed triangles (MT_{28}).

Load-Displacement curves of tension tests are shown in Figure A.3.

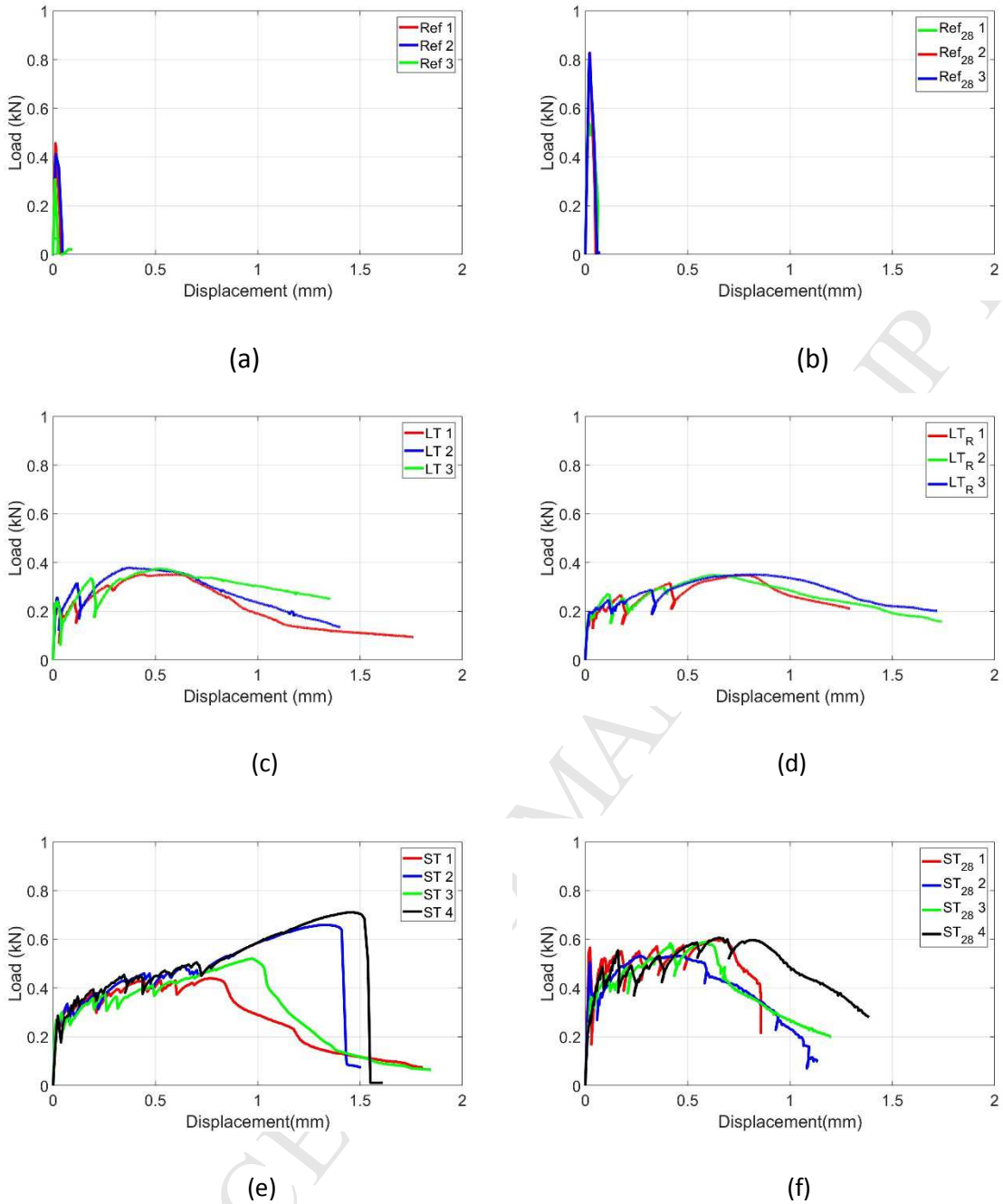

Figure A.3 Tensile Load-displacement curves. (a) reference (no reinforcement) at 7d; (b) reference (no reinforcement) at 28d; (c) large triangles at 7d (LT); (d) large triangles with a rough surface at 7d (LT_R); (e) small triangles at 7d (ST); (f) small triangles at 28d (ST_{28}).

References:

1. Bertolini, L., Elsener, B., Pedeferri, P., Redaelli, E., & Polder, R. (2013). *Corrosion of steel in concrete* (Vol. 392). Weinheim, Germany: Wiley-Vch.
2. Šavija, B., & Luković, M. (2016). Carbonation of cement paste: understanding, challenges, and opportunities. Construction and Building Materials, 117, 285-301.
3. Stefanoni, M., Angst, U., & Elsener, B. (2018). Corrosion rate of carbon steel in carbonated concrete–A critical review. Cement and Concrete Research, 103, 35-48.

4. Neville, A., Chloride attack of reinforced concrete: an overview. Materials and Structures, 1995. 28(2): p. 63.
5. Gonzalez, J. A., Andrade, C., Alonso, C., & Feliu, S. (1995). Comparison of rates of general corrosion and maximum pitting penetration on concrete embedded steel reinforcement. Cement and concrete research, 25(2), 257-264.
6. Šavija, B., Luković, M., Hosseini, S. A. S., Pacheco, J., & Schlangen, E. (2015). Corrosion induced cover cracking studied by X-ray computed tomography, nanoindentation, and energy dispersive X-ray spectrometry (EDS). Materials and Structures, 48(7), 2043-2062.
7. Šavija, B., Luković, M., Pacheco, J., & Schlangen, E. (2013). Cracking of the concrete cover due to reinforcement corrosion: a two-dimensional lattice model study. Construction and Building Materials, 44, 626-638.
8. Šavija, B., Luković, M., & Schlangen, E. (2016). Influence of cracking on moisture uptake in strain-hardening cementitious composites. Journal of Nanomechanics and Micromechanics, 7(1), 04016010.
9. De Schutter, G. (1999). Quantification of the influence of cracks in concrete structures on carbonation and chloride penetration. Magazine of Concrete Research, 51(6), 427-435.
10. Win, P. P., Watanabe, M., & Machida, A. (2004). Penetration profile of chloride ion in cracked reinforced concrete. Cement and concrete research, 34(7), 1073-1079.
11. Šavija, B., Schlangen, E., Pacheco, J., Millar, S., Eichler, T., & Wilsch, G. (2014). Chloride ingress in cracked concrete: a laser induced breakdown spectroscopy (LIBS) study. Journal of Advanced Concrete Technology, 12(10), 425-442.
12. Blagojevic, A. (2016). The influence of cracks on the durability and service life of reinforced concrete structures in relation to chloride-induced corrosion. Technical University of Delft, Delft, The Netherlands.
13. Markovich, I., Van Mier, J. G. M., & Walraven, J. C. (2001). Single fiber pullout from hybrid fiber reinforced concrete. Heron, 46(3), 191-200.
14. Kurihara, N., Kunieda, M., Kamada, T., Uchida, Y., & Rokugo, K. (2000). Tension softening diagrams and evaluation of properties of steel fiber reinforced concrete. Engineering Fracture Mechanics, 65(2-3), 235-245.
15. Purnell, P., & Beddows, J. (2005). Durability and simulated ageing of new matrix glass fibre reinforced concrete. Cement and Concrete Composites, 27(9-10), 875-884.
16. Savastano Jr, H., Santos, S. F., Radonjic, M., & Soboyejo, W. O. (2009). Fracture and fatigue of natural fiber-reinforced cementitious composites. Cement and Concrete Composites, 31(4), 232-243.
17. Li, V. C. (1993). From micromechanics to structural engineering-the design of cementitous composites for civil engineering applications.
18. Li, V. C. (2003). On engineered cementitious composites (ECC). Journal of advanced concrete technology, 1(3), 215-230.
19. Lukovic, M. (2016). Influence of interface and strain hardening cementitious composite (SHCC) properties on the performance of concrete repairs.
20. Zhou, J., Qian, S., Beltran, M. G. S., Ye, G., van Breugel, K., & Li, V. C. (2010). Development of engineered cementitious composites with limestone powder and blast furnace slag. Materials and Structures, 43(6), 803-814.
21. Kunieda, M., Choonghyun, K., Ueda, N., & Nakamura, H. (2012). Recovery of protective performance of cracked ultra high performance-strain hardening cementitious composites (UHP-SHCC) due to autogenous healing. Journal of Advanced Concrete Technology, 10(9), 313-322.
22. Stähli, P., Custer, R., & van Mier, J. G. (2008). On flow properties, fibre distribution, fibre orientation and flexural behaviour of FRC. Materials and Structures, 41(1), 189-196.
23. Stähli, P., & Van Mier, J. G. (2007). Manufacturing, fibre anisotropy and fracture of hybrid fibre concrete. Engineering fracture mechanics, 74(1-2), 223-242.

24. Hartig, J., Häußler-Combe, U., & Schicktanz, K. (2008). Influence of bond properties on the tensile behaviour of Textile Reinforced Concrete. Cement and concrete composites, 30(10), 898-906.
25. Hegger, J., Will, N., Bruckermann, O., & Voss, S. (2006). Load–bearing behaviour and simulation of textile reinforced concrete. Materials and structures, 39(8), 765-776.
26. Mueller, B. (2012). Additive manufacturing technologies–Rapid prototyping to direct digital manufacturing. Assembly Automation, 32(2).
27. Mohamed, O. A., Masood, S. H., & Bhowmik, J. L. (2015). Optimization of fused deposition modeling process parameters: a review of current research and future prospects. Advances in Manufacturing, 3(1), 42-53.
28. Boparai, K. S., Singh, R., & Singh, H. (2016). Development of rapid tooling using fused deposition modeling: a review. Rapid Prototyping Journal, 22(2), 281-299.
29. Bos, F., Wolfs, R., Ahmed, Z., & Salet, T. (2016). Additive manufacturing of concrete in construction: potentials and challenges of 3D concrete printing. Virtual and Physical Prototyping, 11(3), 209-225.
30. Mechtcherine, V., Grafe, J., Nerella, V. N., Spaniol, E., Hertel, M., & Füssel, U. (2018). 3D-printed steel reinforcement for digital concrete construction–Manufacture, mechanical properties and bond behaviour. Construction and Building Materials, 179, 125-137.
31. Farina, I., Fabbrocino, F., Carpentieri, G., Modano, M., Amendola, A., Goodall, R., ... & Fraternali, F. (2016). On the reinforcement of cement mortars through 3D printed polymeric and metallic fibers. Composites Part B: Engineering, 90, 76-85.
32. Nam, Y. J., Hwang, Y. K., Park, J. W., & Lim, Y. M. (2018). Feasibility study to control fiber distribution for enhancement of composite properties via three-dimensional printing. Mechanics of Advanced Materials and Structures, 1-5.
33. Rosewitz, J. A., Choshali, H. A., & Rahbar, N. (2019). Bioinspired design of architected cement-polymer composites. Cement and Concrete Composites, 96, 252-265.
34. Sliseris, J. (2018). Numerical analysis of reinforced concrete structures with oriented steel fibers and re-bars. Engineering Fracture Mechanics, 194, 337-349.
35. Luković, M., Dong, H., Šavija, B., Schlangen, E., Ye, G., & van Breugel, K. (2014). Tailoring strain-hardening cementitious composite repair systems through numerical experimentation. Cement and Concrete Composites, 53, 200-213.
36. Shang, J., Wittmann, F. H., & Zhao, T. PROPERTIES OF SHCC PRODUCED WITH NATURAL FIBRES. In 3rd International RILEM Conference on Strain Hardening Cementitious Composites (p. 179).
37. Zou, R., Xia, Y., Liu, S., Hu, P., Hou, W., Hu, Q., & Shan, C. (2016). Isotropic and anisotropic elasticity and yielding of 3D printed material. Composites Part B: Engineering, 99, 506-513.
38. Xu, Y., Zhang, H., Šavija, B., Figueiredo, S. C., & Schlangen, E. (2019). Deformation and fracture of 3D printed disordered lattice materials: Experiments and modeling. Materials & Design, 162, 143-153.
39. Šavija, B., Luković, M., Kotteman, G. M., Figuieredo, S. C., de Mendoça Filho, F. F., & Schlangen, E. (2017). Development of ductile cementitious composites incorporating microencapsulated phase change materials. International Journal of Advances in Engineering Sciences and Applied Mathematics, 9(3), 169-180.
40. Schlangen, E., & Garboczi, E. J. (1997). Fracture simulations of concrete using lattice models: computational aspects. Engineering fracture mechanics, 57(2-3), 319-332.
41. Van Mier, J. G. (2012). Concrete fracture: a multiscale approach. CRC press.
42. Kanda, T., & Li, V. C. (1999). New micromechanics design theory for pseudostrain hardening cementitious composite. Journal of engineering mechanics, 125(4), 373-381.